Article

Tumour evolution and microenvironment interactions in 2D and 3D space

https://doi.org/10.1038/s41586-024-08087-4

Received: 2 November 2023

Accepted: 19 September 2024

Published online: 30 October 2024

Open access

Check for updates

Chia-Kuei Mo[1,2,19], Jingxian Liu[1,2,19], Siqi Chen[1,2,20], Erik Storrs[1,2,20], Andre Luiz N. Targino da Costa[1,2,20], Andrew Houston[1,2,20], Michael C. Wendl[1,2], Reyka G. Jayasinghe[1,2], Michael D. Iglesia[1,2], Cong Ma[3], John M. Herndon[4,5], Austin N. Southard-Smith[1,2], Xinhao Liu[3], Jacqueline Mudd[4], Alla Karpova[1,2], Andrew Shinkle[1,2], S. Peter Goedegebuure[4,5], Abdurrahman Taha Mousa Ali Abdelzaher[4,5], Peng Bo[1,5], Lauren Fulghum[1,2], Samantha Livingston[1,2], Metin Balaban[3], Angela Hill[4,5], Joseph E. Ippolito[6], Vesteinn Thorsson[7], Jason M. Held[5,8], Ian S. Hagemann[9,10], Eric H. Kim[11], Peter O. Bayguinov[12], Albert H. Kim[5,13], Mary M. Mullen[14], Kooresh I. Shoghi[5,6], Tao Ju[15], Melissa A. Reimers[8], Cody Weimholt[9], Liang-I Kang[9], Sidharth V. Puram[5,16,17], Deborah J. Veis[1,5,9], Russell Pachynski[1,5], Katherine C. Fuh[10,18], Milan G. Chheda[1,5], William E. Gillanders[4,5]✉, Ryan C. Fields[4,5]✉, Benjamin J. Raphael[3]✉, Feng Chen[1,5]✉ & Li Ding[1,2,5,16]✉

To study the spatial interactions among cancer and non-cancer cells[1], we here examined a cohort of 131 tumour sections from 78 cases across 6 cancer types by Visium spatial transcriptomics (ST). This was combined with 48 matched single-nucleus RNA sequencing samples and 22 matched co-detection by indexing (CODEX) samples. To describe tumour structures and habitats, we defined 'tumour microregions' as spatially distinct cancer cell clusters separated by stromal components. They varied in size and density among cancer types, with the largest microregions observed in metastatic samples. We further grouped microregions with shared genetic alterations into 'spatial subclones'. Thirty five tumour sections exhibited subclonal structures. Spatial subclones with distinct copy number variations and mutations displayed differential oncogenic activities. We identified increased metabolic activity at the centre and increased antigen presentation along the leading edges of microregions. We also observed variable T cell infiltrations within microregions and macrophages predominantly residing at tumour boundaries. We reconstructed 3D tumour structures by co-registering 48 serial ST sections from 16 samples, which provided insights into the spatial organization and heterogeneity of tumours. Additionally, using an unsupervised deep-learning algorithm and integrating ST and CODEX data, we identified both immune hot and cold neighbourhoods and enhanced immune exhaustion markers surrounding the 3D subclones. These findings contribute to the understanding of spatial tumour evolution through interactions with the local microenvironment in 2D and 3D space, providing valuable insights into tumour biology.

Treatment-resistant subclones often arise in cancer[2,3], and the tumour microenvironment (TME) can further drive resistance through multiple mechanisms[4,5]. Neither bulk[6] nor single-cell technologies[7] preserve the spatial information necessary to understand these dynamics, but ST[8] instruments, such as Visium[9], can resolve tumour substructures. ST data have been integrated with other data types to examine fine-scale clonal structure and to identify cell–cell interactions (CCIs) with the microenvironment[10]. CODEX multiplex imaging[11] can further complement ST methods by spatially localizing proteins.

Clonal evolution remains one of the most intractable problems of cancer[12]. That is, the spatial and temporal adaptation of a tumour to environmental and treatment stimuli through mutation accumulation and fitness-based selection[12,13]. Previous studies have concentrated on inferring evolutionary history through mutations, but newer technologies, including those mentioned above, have enabled substantially deeper investigations of spatial clonal dynamics[14,15]. The prospect of applying several such technologies to a large, well-powered, cross-cancer cohort to further investigate these phenomena motivates the current work.

Here we report the comprehensive characterization of 131 tumour ST sections across 6 different cancers: breast cancer (BRCA), colorectal carcinoma (CRC), pancreatic ductal adenocarcinoma (PDAC), renal cell carcinoma (RCC), uterine corpus endometrial carcinoma (UCEC) and cholangiocarcinoma (CHOL). We use an approach that combines ST, CODEX and bulk sequencing data and single-cell sequencing data of matching samples to profile spatially distinct tumour regions separated

A list of affiliations appears at the end of the paper.

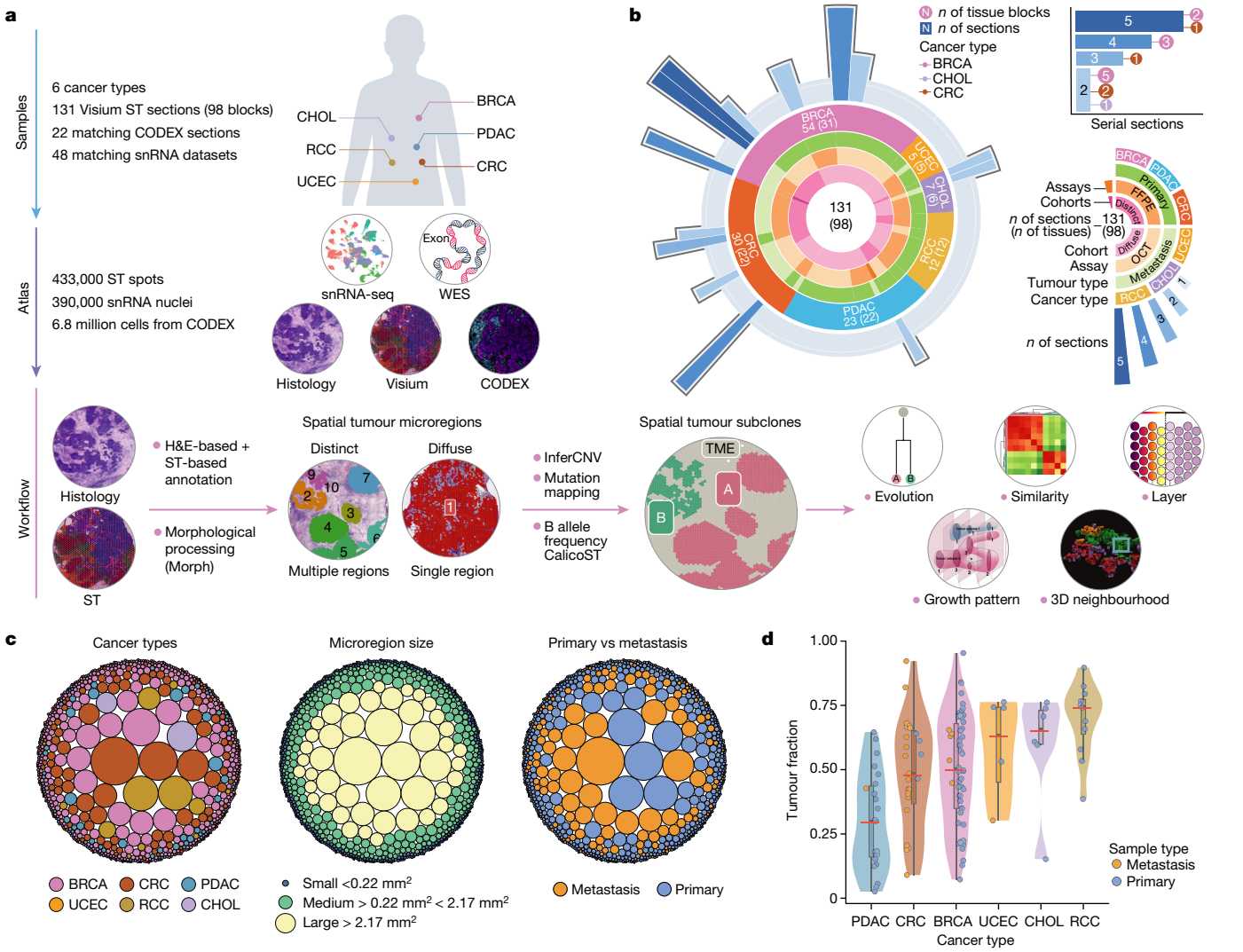

Fig. 1 | Definition of tumour spatial microregions. a, Sample, data type and workflow overview of the spatial subclone cohort of 131 Visium ST sections from 6 different cancer types with 22 and 48 respective matching CODEX and snRNA datasets. Data encompass 54 BRCA, 30 CRC, 23 PDAC, 12 RCC, 5 UCEC and 7 CHOL samples. Bottom, workflow for generating spatial tumour microregions, inferring spatial tumour subclones and conducting downstream analyses. Based on the distribution of tumour regions, we separated samples into spatially distinct and spatially diffuse cohorts. Analyses included tumour subclone evolution analysis, transcriptional similarity and layer-based TME interactions, tumour growth pattern construction, and multisection 3D neighbourhood reconstructions using custom code (Methods). **b**, Circular cohort overview plot at the tissue block level. The outcrop height of the outermost ring indicates the number of sections per tissue block. The top right insert shows a legend, with numbers in bubbles indicating counts of tissue blocks with a given number of serial sections. Successive rings indicate the cancer type annotated with section (tissue block) counts, tumour type, assay type and spatial cohort designation. **c**, Microregion distribution in the spatially distinct cohort at the section level coloured by cancer type (left), microregion size group (middle) and primary versus metastasis (right). Each circle indicates one microregion. The size of each circle represents the size of the microregion. **d**, Tumour versus stromal–immune spot fractions across cancer types for the entire cohort at the section level. Each point represents a sample, coloured by type: primary ($n = 98$ sections from 60 cases) or metastatic ($n = 33$ sections from 16 cases). The box plot's centre line represents the median, with the lower and upper hinges indicating the first and third quartiles. Whiskers extend to the highest and lowest values within 1.5 times the interquartile range (IQR) from the hinges.

by stromal components, which we call 'tumour microregions'. We demonstrate that there are distinct genetic clones within these microregions with specific copy number variations (CNVs) and with differential activity within oncogenic pathways, particularly the MYC pathway. Notably, we show that immune–tumour and stromal–tumour interactions vary among these tumour regions. Additionally, our study highlights distinct characteristics between primary and metastatic tumours, including differences in tumour growth patterns and transcriptional profiles. To further support our findings showing that immune populations in the TME surround specific spatial tumour regions, we use CODEX and a multimodal 3D reconstruction tool trained on adjacent ST sections. The results confirm the connectivity of subclones and microregions in different sections within 3D space. These reconstructions highlight tumour–immune interphase niches and interactions. Overall, this spatial omics approach provides deeper insights into clonal evolution and the microregional distinctions across six different solid tumour types, paving the way to continued advances in understanding the mechanisms of therapeutic resistance in cancer.

Spatial microregions across cancers

We profiled 131 tumour sections with ST data from 98 blocks spanning 6 cancer types as part of the NCI's Human Tumor Atlas Network: 54 BRCA, 30 CRC, 23 PDAC, 12 RCC, 5 UCEC and 7 CHOL (Fig. 1a, Extended Data Fig. 1 and Supplementary Table 1) from 78 cases (22, 17, 16, 12, 5 and 6 cases, respectively). Three RCC samples were from the Clinical

Proteomics Tumour Analysis Consortium. Using histological haematoxylin and eosin (H&E) staining and transcriptional profiles, we identified tumour microregions as spatially distinct cancer cell clusters separated by stromal areas (Methods) and designated Visium spots as malignant or non-malignant. We used the Morph toolset to subsequently refine tumour boundaries, determine distances of spots from boundaries and construct layers of spots, indexing their depths to tumour boundaries (Methods). We selected 50 sections with multiple tumour regions as the 'spatially distinct cohort' (Extended Data Fig. 2) and 82 samples with diffuse tumour regions as the 'spatially diffuse cohort' (Extended Data Fig. 3). We also produced serial sections of 15 tumour tissue blocks, which resulted in 48 sections suitable for 3D tumour reconstruction (Fig. 1b and Extended Data Fig. 4a).

Based on the estimated area per tumour microregion (Methods), we categorized microregion sizes as small (<25 spots or 0.22 mm^2), medium (25–250 spots or 0.22–2.17 mm^2) or large (>250 spots or 2.17 mm^2) (Fig. 1d). CRC had larger microregions (average of 2.9 layers) than BRCA (average of 2.1 layers; false discovery rate (FDR) = 0.00035, Welch's *t*-test) and PDAC (average of 2.37 layers; FDR = 0.032, Welch's *t*-test). Conversely, BRCA and PDAC microregion depths were statistically indistinguishable ($P = 0.18$, Welch's *t*-test). RCC had the highest tumour fraction, whereas PDAC had the lowest (Fig. 1c), which is probably due to the higher stromal content and lower tumour cell density in PDAC[16], which in turn leads to smaller microregion sizes. Primary tumours generally had more small microregions (66.3%) compared to metastases (40.2%), which had more medium-sized microregions (43.2%) (Extended Data Fig. 4b,c). Larger microregions were predominantly found in metastases (16.3% compared with 3.2% in primary), which also had deeper microregions than primary tumours (3.4 compared with 1.9 layers; Welch's *t*-test FDR < 10^{-14}). This difference held for BRCA-only sections (FDR < 10^{-14}), for which we had data for both metastases (5 sections, 44 microregions, mean depth of 4.2) and primary tumours (8 sections, 222 microregions, mean depth of 1.7). These results suggest that there is divergent growth between primary and metastatic tumours and an organ-specific TME effect on microregion growth and organization. Examples include samples HT268B1-Th1H3 (BRCA liver metastasis) and HT260C1-Th1K1U1 (CRC liver metastasis), which had large regions occupying 3–4 mm^2 (400–500 spots), whereas sample HT270P1-H2U1 (PDAC) had a smaller (mean of 0.2 mm^2 or 26 spots) but greater number of microregions ($n = 24$) (Extended Data Fig. 4d–h). In the spatially distinct cohort, samples with the highest microregion counts were from BRCA blocks rich in ductal carcinoma in situ (DCIS) (HT397B1-S1H2, HT339B1-S1H3 and HT206B1-S1; Extended Data Fig. 4d). This distribution could reflect the tendency of ductal cancer cells to grow along the secretion duct in both organs, which may explain our observation of numerous small regions.

Focal clonal evolution in microregions

We discerned genome-wide CNVs using CalicoST and InferCNV (Supplementary Fig. 1 and Methods), selecting confident events in each microregion by filtering those in matching whole-exome sequencing (WES) data (Supplementary Table 2). We then clustered microregions into spatial subclones based on CNV similarity (Fig. 2a and Methods). We detected spatial CNVs in 125 out of the 131 sections, out of which we observed 1–3 subclones per section (about 6.5 × 6.5 mm, 72% with a single clone, 20% with 2 subclones and 8% with 3 subclones) (Fig. 2b). A single clone can be composed of subclones that our workflow cannot detect, such as subclones intermixed in the same microregion and subclones differentiated by genetic alterations not covered by the Visium transcriptome. Within these limitations, we identified multiple spatial subclones in sections from 4 cancer types: BRCA (17 sections), PDAC (10 sections), CRC (6 sections) and RCC (2 sections). CNV profiles of spatial subclones were compared with matching WES data and showed high genome-wide similarity (Methods and Extended Data Fig. 5a). We also mapped somatic mutations onto optimal cutting temperature (OCT)-embedded ST sections, for which each section showed 1–98 mutations mapped specifically in tumour regions (Fig. 2c and Extended Data Fig. 5b).

Sample HT260C1 (CRC liver metastasis) contained 12 tumour microregions, which mapped to 2 spatial subclones (Fig. 2d). Both clonal events (chromosome 13 amplification and chromosome 8p deletion), as well as several subclonal events (amplifications in chromosomes 6p, 12p and 20q in clone c2, and amplification of chromosome 12q in clone c1), were identified and confirmed with matching single-nucleus RNA sequencing (snRNA-seq) data and WES-based CNV inference (Fig. 2e,f). Although histology indicated a fibrotic separation between the two subclones, multiple shared clonal CNVs suggested a common origin (Fig. 2g). Somatic variants from transcripts provided further supporting evidence for tumour clonality. In addition, 17 WES-based somatic mutations were mapped to ST (Extended Data Fig. 5c). Several mutations showed differential variant allele frequency (VAF) in tumour regions compared with normal regions (Extended Data Fig. 5c, left) and differential VAFs between the two subclones (Extended Data Fig. 5c, right). Both subclones showed *LDHB* expression, and a VAF for mutation *LDHB* c.921G>A was significantly higher in subclone c2 than in c1 (Fig. 2h,i; $P = 6.58 \times 10^{-6}$, two-sided proportion test). Using Xenium data, we analysed both *LDHB* wild-type (WT) and c.921G>A alleles on a matching tumour section, the WT allele in both subclones and the mutant allele in subclone c2 (Fig. 2j). Subclone c2 diverged from c1, with a gain of unique genetic alterations in both CNV and mutations. Similarly, a BRCA liver metastasis sample, HT268B1, showed two distinct spatial subclones that were supported by matching snRNA-seq data, with chromosomal-arm-level CNV differences (Extended Data Fig. 5d–g) and subclonal mutations (Extended Data Fig. 5h). For example, *EEF1A1* was expressed in both spatial clones, whereas mutation *EEF1A1* 1324G>C was specifically observed in subclone c2 (proportion test FDR < 0.05; Extended Data Fig. 5i,j).

Primary PDAC samples, despite their smaller microregions, also contained multiple spatial subclones. Sample HT270P1 showed three subclones across two sections from two tumour blocks with OCT and formalin-fixed paraffin-embedded (FFPE) preservation, respectively (Supplementary Fig. 2a). Most primary BRCA cases showed that all tumour microregions belonged to a single genetic clone, such as HT206B1 across five serial sections (Supplementary Fig. 1b). In seven out of nine cases, a single subclone encompassed both DCIS and invasive ductal carcinoma (IDC) morphology, which indicated that the transition between them happens without large copy number alterations (Supplementary Fig. 2b). However, primary BRCA sample HT397B1 showed three spatial subclones across four sections from two tumour blocks (Supplementary Fig. 2a). Two of the clones showed both DCIS and IDC morphologies, whereas clone 3 only showed IDC morphology, which indicated a parallel transition from DCIS to IDC between the spatial subclones (Supplementary Fig. 2b).

Single-nucleotide polymorphisms reveal copy-number-neutral loss of heterozygosity that is missed by read-depth inference alone. A CRC liver metastasis sample (HT112C1-Th1) with strong B allele frequency deviation in copy-number-neutral chromosome 21 indicated a subclonal genetic alteration in clone A (Supplementary Fig. 2a). These observations collectively suggest that spatial subclones within a tumour section probably stem from a common ancestor.

Genetic changes drive tumour disparities

To mitigate the influence of infiltrating immune and stromal cells, we first excluded organ-specific, non-malignant cell-type marker genes using snRNA-seq data (Methods). Subsequently, we used an entropy-based method, ROGUE, to analyse transcriptional heterogeneity among tumour microregions (Methods). Our analysis revealed that PDAC had the highest heterogeneity (0.1–0.6), whereas BRCA,

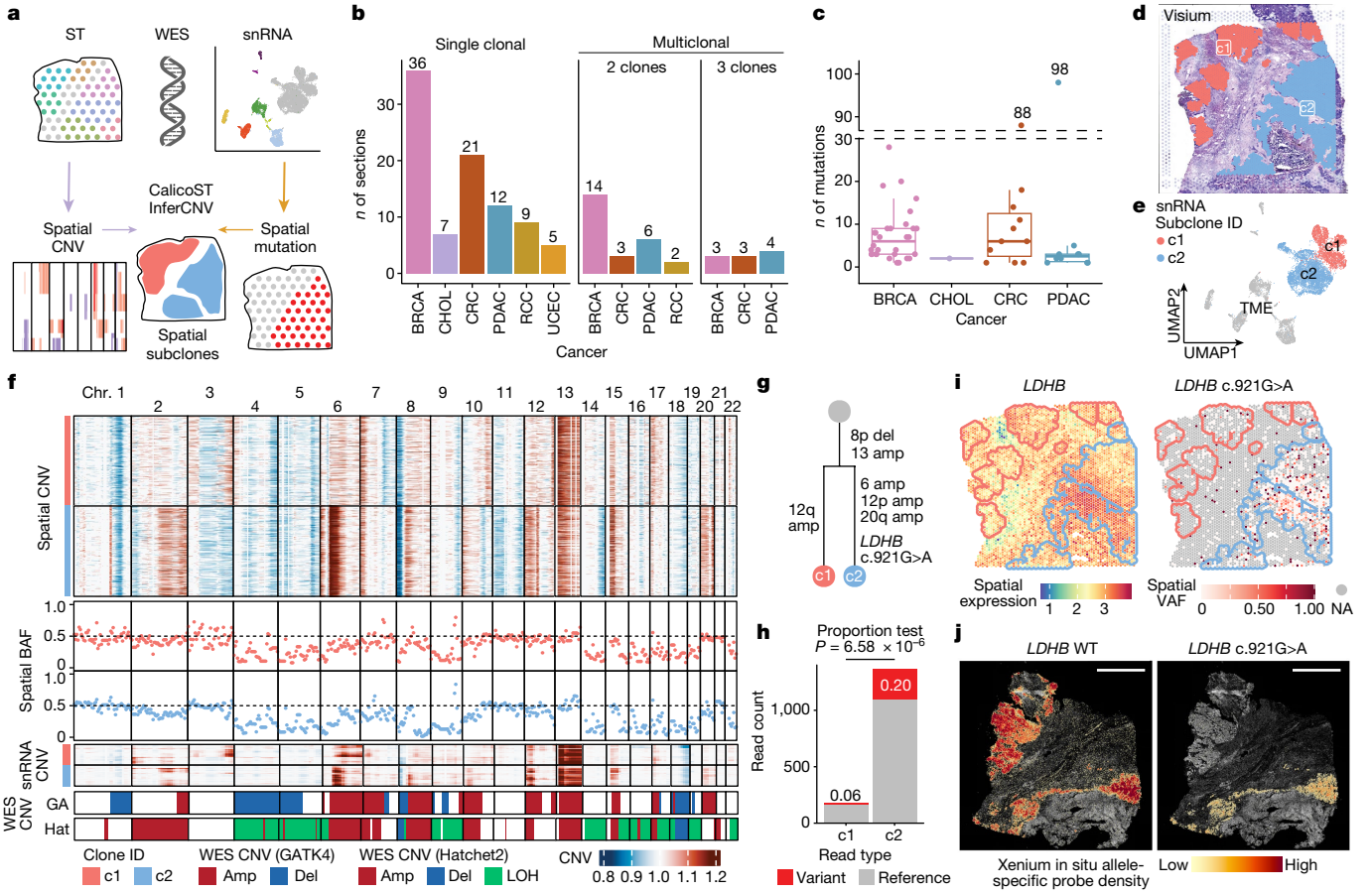

Fig. 2 | Genetic alteration reveals spatial clonal evolution. a, Summary of workflow for identifying spatial subclones. **b**, Numbers of spatial clones detected in each section summarized by cancer type. Multiclonal sections (2 or 3 spatial subclones) are observed in BRCA, CRC, PDAC and RCC in this cohort ($n = 125$ sections from 74 cases with detected CNV). **c**, Spatial somatic mutation mapping per section detected in OCT ST data. WES-derived somatic mutations with significantly higher VAF in tumour regions than non-tumour regions (binomial test, FDR < 0.05) are shown ($n = 60$ OCT sections from 29 cases). The box plot's centre line represents the median, with the lower and upper hinges indicating the first and third quartiles. Whiskers extend to the highest and lowest values within 1.5 times the IQR from the hinges. **d**,**e**, A colorectal cancer liver metastasis sample (HT260C1) with 12 tumour microregions demonstrates 2 tumour subclones, c1 and c2, separated spatially (**d**), with support from matching snRNA-seq data (**e**). **f**, Heatmap of estimated somatic CNVs per spot shows both shared and unique CNV events between the two spatial subclones. The B allele frequencies (BAFs) in each spatial subclone from the same genomic window are shown in the middle tracks and corresponding snRNA-inferred and WES-inferred CNV statuses using GATK4 (GA) and Hatchet2 (Hat) are shown in the bottom tracks. **g**, The predicted phylogenetic relationship of c1 and c2. **h**, The VAF for mutation *LDHB* c.921G>A is significantly higher in c2 than c1 ($P = 6.58 \times 10^{-6}$, two-sided proportion test). **i**, Subclonal mutation *LDHB* c.921G>A is uniquely detected in clone 2 in spatial transcriptomics, whereas *LDHB* expression is in both spatial subclones. **j**, Xenium in situ allele-specific probe density shows the WT allele of *LDHB* in both subclones and the mutant allele uniquely in the right subclone (c2). Scale bars, 2 mm. amp, amplification; del, deletion; LOH, loss of heterozygosity; NA, not applicable; UMAP, uniform manifold approximation and projection.

CRC, RCC and UCEC had moderate levels (0.05–0.45), and CHOL had the lowest levels (<0.2) (Extended Data Fig. 6a). To further investigate the effect of genetic alterations and microenvironmental adaptations on transcriptional profiles, we assessed transcriptional similarity using pairwise Pearson correlation among tumour microregions (Methods), comparing within and between different genetic clones. We observed greater similarity within subclones (Extended Data Fig. 6b, green) compared with between different subclones (Extended Data Fig. 6b, orange) across all samples from BRCA, CRC, PDAC and RCC (Extended Data Fig. 6b and Methods). This pattern remained consistent in both primary and metastatic samples in BRCA and CRC, which underscores the central role of genetic composition in shaping transcriptional similarities across microregions.

To understand the activation of oncogenic pathways across microregions, we performed gene set enrichment analysis (GSEA) with differentially expressed genes (DEGs) between tumour microregions and stroma regions (Methods). Our analysis identified common pathways such as MYC and E2F shared across microregions, but distinct pathways, such as the unfolded protein response, that was specific to some microregions in sample HT268B1 (BRCA metastasis) (Extended Data Fig. 7a–f). Here genetic alterations controlled the transcriptional profile, whereas in other samples, subtle variations arose from the local microenvironment or undetected genetic events. For example, sample HT260C1 showed two subclones with distinct copy number profiles (Fig. 2d), whereas microregions within clone 1 had varying expression similarities, despite having similar CNVs (Extended Data Fig. 6c, indicated by the dotted boxes).

When applying GSEA to identify subclone-specific pathways, we found varied microregional expression levels within the G2M checkpoint pathway in clone 1 (Extended Data Figs. 6d and 7g,h, indicated by the dotted boxes) in sample HT260C1. This pattern was mirrored in MYC for both metastasis samples HT260C1 and HT268B1, with distinct sets of MYC downstream genes among tumour subclones (Extended Data Fig. 7e,f,i,j and Supplementary Fig. 3). This result underscores the complexity of this pathway, which is commonly dysregulated in cancer and influences many oncogenic processes[17]. Clone 2 of HT260C1 had

an enrichment of translation initiation complex (eIF family) and G1S progression (CDK4), whereas clone 1 had DNA replication genes (MCM family) (Extended Data Fig. 7i).

Enrichment tests using Enrichr with the drug perturbation dataset LINCS L1000 (Methods) predicted varying treatment responses of subclones (Supplementary Fig. 4). For instance, all subclones in HT397B1-S1H3 and HT112C1-Th1 should respond to the mTOR inhibitor torin-2, but only clone 1, not clone 2, in HT268B1-Th1K3 responded. This variation underscores the importance of profiling spatial subclones.

Cellular pathways at the tumour core and edge

We further investigated whether different transcriptional programs exist in tumour microregion centres (cores) compared to their leading edges (interfaces between the tumour and the TME–stroma). To that end, we used Morph to measure the distance of each tumour spot to its nearest tumour–TME border (Methods and Extended Data Fig. 8a). The relationship between the total layer depth of a microregion and its size (total area measured as the number of spots occupied) describes the general shape of the region (Extended Data Fig. 8b). The dashed reference line indicates the depth–size relationship of perfectly circular regions. For all five cancer types in the spatially distinct cohort ($n = 50$), smaller regions tended to exhibit near-circular shapes. But as the layer depth increased, regions tended to deviate from their circular shape, and an expanded interface between tumour and non-tumour cells arose.

Spatial gene expression profiles can also be characterized in terms of layer depth. For each layer-assigned spot, we independently performed a linear regression between gene expression and spot depth for each gene. Tumour purity estimates using the methods RCTD[18] or ESTIMATE[19] were included as a covariate to adjust for possible purity decreases towards section edges (Methods). A positive correlation with depth indicates increased gene expression towards the tumour core and vice versa. In the CRC metastasis sample HT260C1, the top centre-enriched genes (*CKB* and *VEGFA*) and periphery-enriched genes (*HSP90AB1* and *LDHB*) are shown with the regression line and spatial expression pattern in Extended Data Fig. 6e,f. Also shown are respective top centre-enriched (*NDRG1*, *S100A2* and *CA9*) and periphery-enriched genes (*TUBA1B*, *NDUFA4* and *TOMM40*) for HT206C1 in Extended Data Fig. 8c–e. These results were supported by snRNA-seq data from matching tumour samples, which demonstrates that the top shared genes are mainly expressed by malignant cells, with small contributions from immune and stroma cells (Supplementary Fig. 5a–d).

We subsequently identified genes recurrently enriched in tumour centres and in peripheries across cases (Extended Data Fig. 6g). Top shared centre-enriched genes were involved in ribosome assembly (RPL and RPS family genes such as *RPS4X*, *RPL22* and *RPL4*), along with genes such as *TXN*[20], *C5orf46* (ref. 21) and the long non-coding RNA *SNHG29* (ref. 22), which are linked to tumour growth in various cancer types. By contrast, the tumour periphery was enriched in the following genes: a different set of ribosomal RPL and RPS genes (*RPL35*, *RPLP1* and *RPS27*); *ENO1*, a multifunctional oncoprotein involved in glycolysis, invasion and immunosuppression[23]; *TMSB10*, which promotes proliferation and invasion in BRCA[24]; and *ISG15*, which induces the formation of M2 macrophages[25]. These differential biological processes indicate that malignant cells in the core are actively undergoing protein translation, whereas those at the edges are involved in tumour migration and immune modulation, interfacing with immune and stromal components.

Clonal-specific tumour–TME interactions

To investigate TME composition in tumour boundary regions, we examined the differential infiltration of non-tumour cells between tumour spatial subclones, the location of such infiltration and genes and CCIs enriched in boundary regions (Fig. 3a). We used matching snRNA-seq data as a reference for spot-level cell-type deconvolution and performed pairwise differential infiltration analysis between all spatial subclones of the same sample. Top differential cell types in terms of infiltration included macrophages in BRCA, hepatocytes in CRC and fibroblasts in PDAC (Extended Data Fig. 9a). A primary BRCA sample, HT397B1, with three spatial subclones showed differential infiltration in both T cells and macrophages, with subclone c3 showing the largest fraction of both (Fig. 3b). CODEX data validated the increased level of T cell markers (CD3 and CD8) and the non-T cell immune marker (HLA-DR) staining in subclone c3.

We used the above-described layer assignments to ascertain whether infiltration exhibits spatial patterns, and we defined six ordered regions from the tumour core to the TME: T3+, T2, T1, E1, E2 and E3+. These showed the expected decreasing trend for tumour cells (Extended Data Fig. 9b), but various patterns for non-tumour cells. Macrophages clustered outside the tumour in E1 and E2, whereas T cells showed infiltration both immediately outside (E1 and E2) and inside the tumour (T1 and T2) (Fig. 3c). Both macrophage and T cell fractions were decreased in the distant TME (layer E3+) where fibroblasts dominate, an observation supported by CODEX data (Extended Data Fig. 9c). With an inter-layer distance of only 100 μm, our observation indicates that there is strong spatial recruitment of immune cells by tumours at the microscopic level.

We also performed differential expression analysis between the boundary regions T1 and E1 and with all other spots (Fig. 3d). Top boundary genes shared across samples and cancer types included genes of extracellular matrix proteins (*POSTN* and *FN1*) and interferon-induced macrophage activation proteins (*IFI30*) (Extended Data Fig. 9d). Matching snRNA-seq data showed that the top boundary genes had significantly higher expression (adjusted $P < 0.05$, Bonferroni correction) across the cohort in non-tumour cell types (*POSTN*, *FN1* and *TIMP1* in fibroblasts and *IFI30* in macrophages), which suggested that there are interactions between tumour and non-tumour cells at the boundary (Fig. 3d). To quantify spatial CCIs, we ran COMMOT on 18 cases with 39 sections and then discerned differential receiver–sender signals between spots within and outside tumour boundary regions. The top shared CCIs in boundary regions were extracellular matrix (ECM) receptors (collagen, laminin, FN1 and THBS), secreted signalling (SEMA3, SEMA4, ncWNT and MK) and cell–cell adhesion (EPHB and NOTCH) (Fig. 3e). As an example, the MK pathway was observed in CRC, PDAC and BRCA samples, for which the signal goes from malignant cell regions to the TME interface (Extended Data Fig. 9e). The pathway included interactions between the ligand MDK and the receptors NCL and SDC4 (ref. 26). Malignant cells secrete MDK to create an immunosuppressive and angiogenic environment[27], which in turn promotes tumour growth. We also found ECM pathways for which the signal goes from the TME towards malignant cell regions. One of the top interactions, the THBS pathway, describes ECM components *THBS1–THBS4* (which encodes thrombospondin) binding to cell surface receptors *CD36* and *CD47*, which in turn modulate cell adhesion, proliferation and angiogenesis[28–30]. Enrichment of tumour-associated immune cells, genes and CCIs within 200-μm-wide boundary regions illustrates communication between malignant cells and their environment that would be invisible to spatially agnostic technologies.

3D tumour structure and TME interactions

To investigate tumour growth patterns and TME interactions in 3D, we serially sectioned tumours from BRCA, CRC, PDAC and CHOL, conducting ST on 11 samples and CODEX on 2 samples. Using PASTE2, we co-registered 48 sections from the 11 ST specimens to construct tumour volumes (Fig. 4a and Methods). Our analysis revealed variations in tumour volume numbers among samples, with BRCA showing the highest volume count (Fig. 4b), particularly in samples with

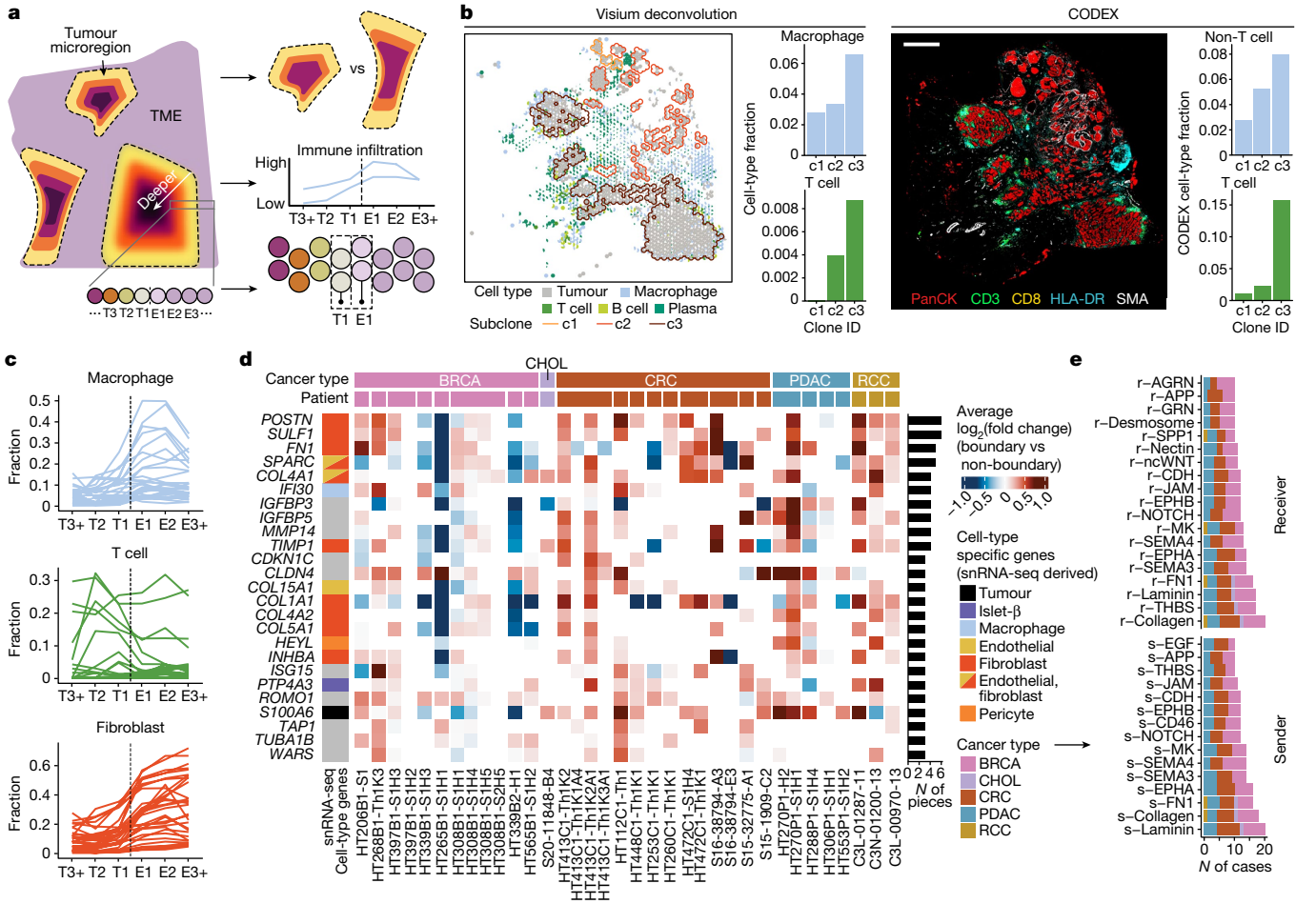

Fig. 3 | Immune and stromal infiltration inside spatial tumour microregions. **a**, Analysis design focusing on the differential infiltration level between spatial subclones and the spatial location of such infiltration with respect to the tumour–TME border. **b**, Left, a primary BRCA sample HT397B1 shows higher macrophage and T cell levels in clone c3. Right, T cell markers (CD3 and CD8) and the non-T cell immune marker (HLA-DR) show higher intensity in the same regions from CODEX data. Scale bar, 1 mm. **c**, Fraction of macrophages, T cells and fibroblasts averaged across microregions in the following layers: T3 and above (T3+), T2, T1, E1, E2, and E3 and above (E3+), in 14 cases. **d**, Genes differentially enriched in the tumour boundary regions. Colour represents the $\log_2$(fold change) of gene expression between boundary regions and non-boundary regions, with non-differential comparisons in white ($n = 25$ spatially distinct cases). Each column represents a tumour block (multisection averaged) and tumour blocks from the same patient were grouped together (no gaps between columns). snRNA-seq-based cell-type specific expression is shown on the left, and the number of tumour blocks with significant enrichment is shown on the right (adjusted $P < 0.05$, Bonferroni correction). **e**, Boundary-enriched CCIs shared across samples ($n = 25$ spatially distinct cases) based on receiver (r)–sender (s) signals.

prominent miniature duct-like tumour growth patterns (HT206B1-S1, 1A–1E; HT339B1-S1H3, 3D and 3E; and HT397B1-S1H3, 4B–4D; Extended Data Fig. 2). By contrast, CHOL, CRC, PDAC and other BRCA sections exhibited more invasive tumours that formed larger, continuous structures that resulted in fewer but larger volumes.

We then analysed these tumour volumes for structural complexity using two topological metrics: (1) connectivity (degree), which measures the number of connections to adjacent microregions, and (2) the number of loops per volume, which indicates instances in which adjacent sections split and merge to form doughnut-shaped structures. The maximum connectivity score serves as an indicator of tumour structural complexity. Of the 15 tumour volumes analysed, 8 (6 BRCA, 1 CHOL and 1 CRC) had a maximum connectivity score exceeding 5, which reflected the frequent formation of complex branching structures in these tumours (Fig. 4c). The highest connectivity score of 11 was observed in CHOL sample HT226C1-Th1, which resulted from a large merged volume in U1 that fragmented into smaller microregions in the adjacent section U2 (Extended Data Fig. 10a,b). Additionally, 5 out of 81 volumes across 15 tumour pieces contained complex loop structures, with the highest loop count of 12 found in volume 14 of sample HT206B1 (Extended Data Fig. 10c). These loops probably result from the interwoven DCIS-like growth pattern in volume 14, as confirmed by its histology (Extended Data Fig. 10d).

We selected a BRCA liver metastasis sample, HT268B1-Th1H3, for detailed 3D volume reconstruction and structural analysis. This sample contained four tumour volumes (volume 1 to volume 4) (Fig. 4d,e). Volumes 1, 3 and 4 formed separate subvolumes within clone 2, which probably connected beyond the approximately 300 µm tissue section examined. Volume 2, the largest and most complex volume, belonged solely to clone 1, with a maximum connectivity of 8 and 6 loops, which indicated substantial branching and merging (Fig. 4d). Histological images of HT268B1 (Extended Data Fig. 2a–e) confirmed visible splitting and merging, thereby demonstrating that even tumours without clear ductal or lobular structures can exhibit diverse growth patterns, invasive behaviour and complex branching.

We next used an unsupervised deep-learning approach to identify 3D cellular neighbourhoods in serial-sectioned ST datasets (Methods). After registration of serial sections, a vision transformer (ViT) autoencoder was trained on ST, CODEX and H&E sections. Annotated image patches were then used to construct 3D cellular neighbourhoods,

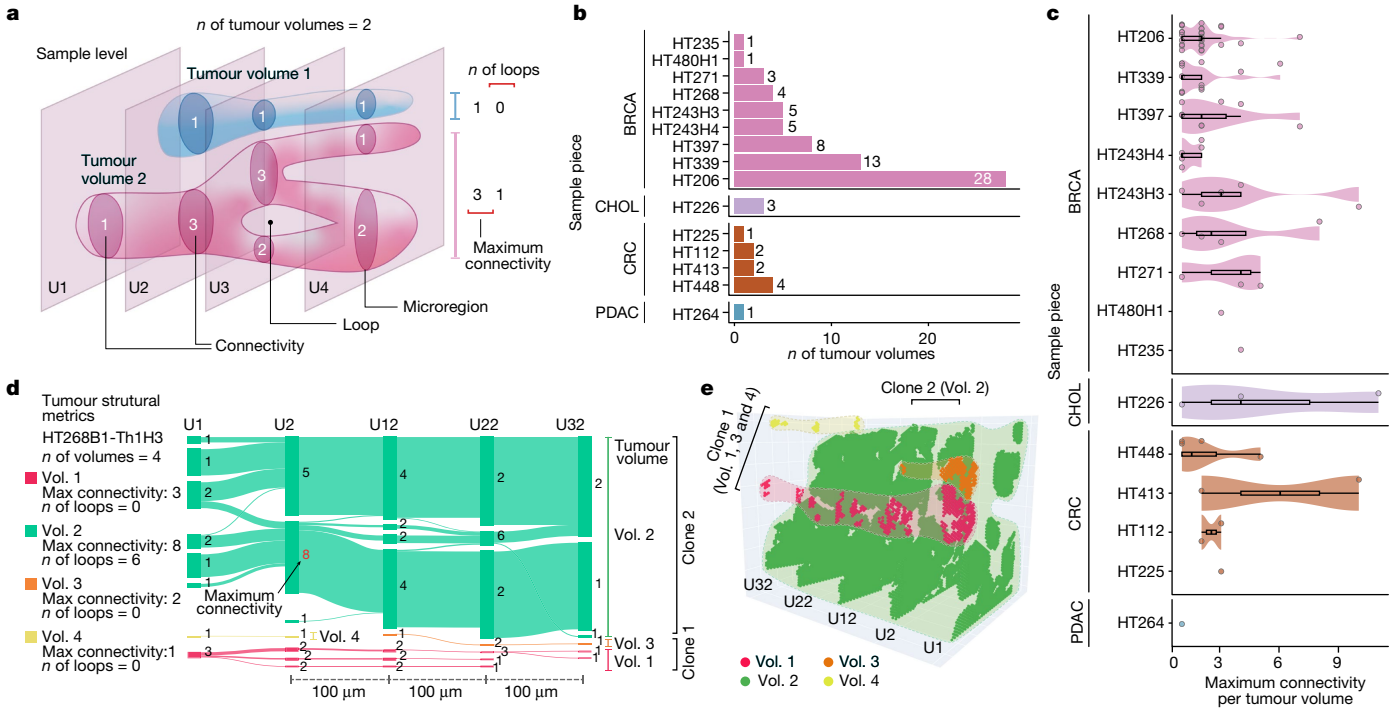

Fig. 4 | 3D tumour volume reconstruction reveals diverse tumour growth patterns. a, Tumour growth pattern diagram with two distinct tumour 3D volumes from four ST sections. The number of tumour volumes, connectivity, maximum connectivity and the number of loops are annotated to illustrate the concept of these geometric quantities. **b**, Number of tumour volumes (components) for each sample piece. **c**, Distribution of maximum connectivity of sample pieces. Each dot represents one tumour volume ($n = 15$ sections from 14 cases). The box plot's centre line represents the median, with the lower and upper hinges indicating the first and third quartiles. Whiskers extend to the highest and lowest values within 1.5 times the IQR from the hinges. **d**, Sankey plot showing tumour microregion connections across sections, with 3D tumour volumes for tissue block HT268B1-Th1H3 (BRCA metastasis). The maximum connectivity of volume 2 (Vol. 2) is highlighted in red. Numbers next to each microregion indicate its connectivity. **e**, Microregion and 3D tumour volume spatial distributions on the ST sections for HT268B1-Th1H3.

which enabled the discovery of these neighbourhoods across multiple sections (Extended Data Fig. 10e and Supplementary Fig. 7b). We applied this approach to a primary BRCA sample HT397B1 (six H&E, four CODEX and two Visium ST sections) and a BRCA liver metastasis sample HT268B1 (four Visium ST sections) (Extended Data Fig. 10f and Supplementary Fig. 7c,d).

In sample HT268B1, neighbourhoods with at least 60% overlap with previously defined spatial subclones (Fig. 2d) were classified as tumour-enriched, with the remainder as TME neighbourhoods (Methods). Two of these neighbourhoods (4 and 6) were in close contact with the periphery of both subclones (Fig. 5a,b). Notably, when viewed in 3D space, the neighbourhoods largely contiguously surround the subclones, except for the upper portion of the block where the neighbourhoods were more broken. We then quantified these two neighbourhoods based on shared and unique DEGs (Fig. 5c), and we found immune responses (*IFI27* and *HLA-DRA*) and stromal (*BST2* and *SPARC*) genes in both. Neighbourhood 4 was enriched in *HMGA1*, which regulates chromatin structure and has a role in malignant cell progression[31,32], and *TYMP*, a factor involved in angiogenesis[33,34]. Neighbourhood 6 was enriched for genes important for immunoregulatory (*CCL19*) and immunoglobulin receptor binding (*IGLC2*, *IGHG1* and *IGKC*), which are prognostic in BRCA[35,36]. In three dimensions, we continued to see clear association of these DEGs, in particular *TYMP1* and *IGLC2*, with clones 1 and 2, respectively, throughout the tissue volume (Fig. 5d and Extended Data Fig. 10g).

The primary BRCA sample HT397B1 had two main regions of TME–tumour morphology: an immune-cold area with both DCIS and IDC morphologies containing clones 1 and 2, and an immune-hot IDC region that harboured clone 3 (Figs. 5e,f and 3b and Supplementary Fig. 2b). We stratified TME neighbourhoods by their contact fraction with clone 3, which highlighted the top and bottom quartiles (Fig. 5e,g). According to CODEX-based cell-type annotations, neighbourhoods associated with clone 3 had a higher fraction of T cells and a decreased fraction of fibroblast cells compared with those near clones 1 and 2, a result that aligned with previous findings (Figs. 5g and 3b). To further verify the immune–stromal status of these neighbourhoods, we selected two regions of interest (ROIs): ROI 1, located in the immune-cold clone 2, and ROI 2, located in the immune-hot clone 3. ROI 1 had low fractions of macrophages, T cells and B cells, whereas ROI 2 had much higher levels of these cell types (Fig. 5f). These trends were also evident in CODEX sections, for which immune markers were more intense in ROI 2. Additionally, ROI 1 showed an increased fibroblast cell fraction, with smooth muscle actin (SMA) highly expressed in the myoepithelium surrounding the tumour regions, a hallmark of DCIS. Our findings indicate that these cell-type associations and DCIS and IDC-like subclones are consistent in three dimensions, based on calculated cell-type densities around the 3D tumour volume and the generation of immune, stromal and epithelial volumes (Fig. 5h and Extended Data Fig. 10h). These analyses demonstrate that 3D reconstruction offers increased sensitivity for investigating heterogeneous tumour microenvironments.

Discussion

This study identified genomically distinct spatial microregions and spatially distributed subclones in samples across solid tumour types. We propose that CNV variability is a major driver of the transcriptional variation seen in these microregions. Spatial subclones identified in the same tumour block shared a common ancestry, a finding congruent with previous studies of tumour evolution[37–39]. A second major driver of variability is exposure to the TME, and we observed distinct

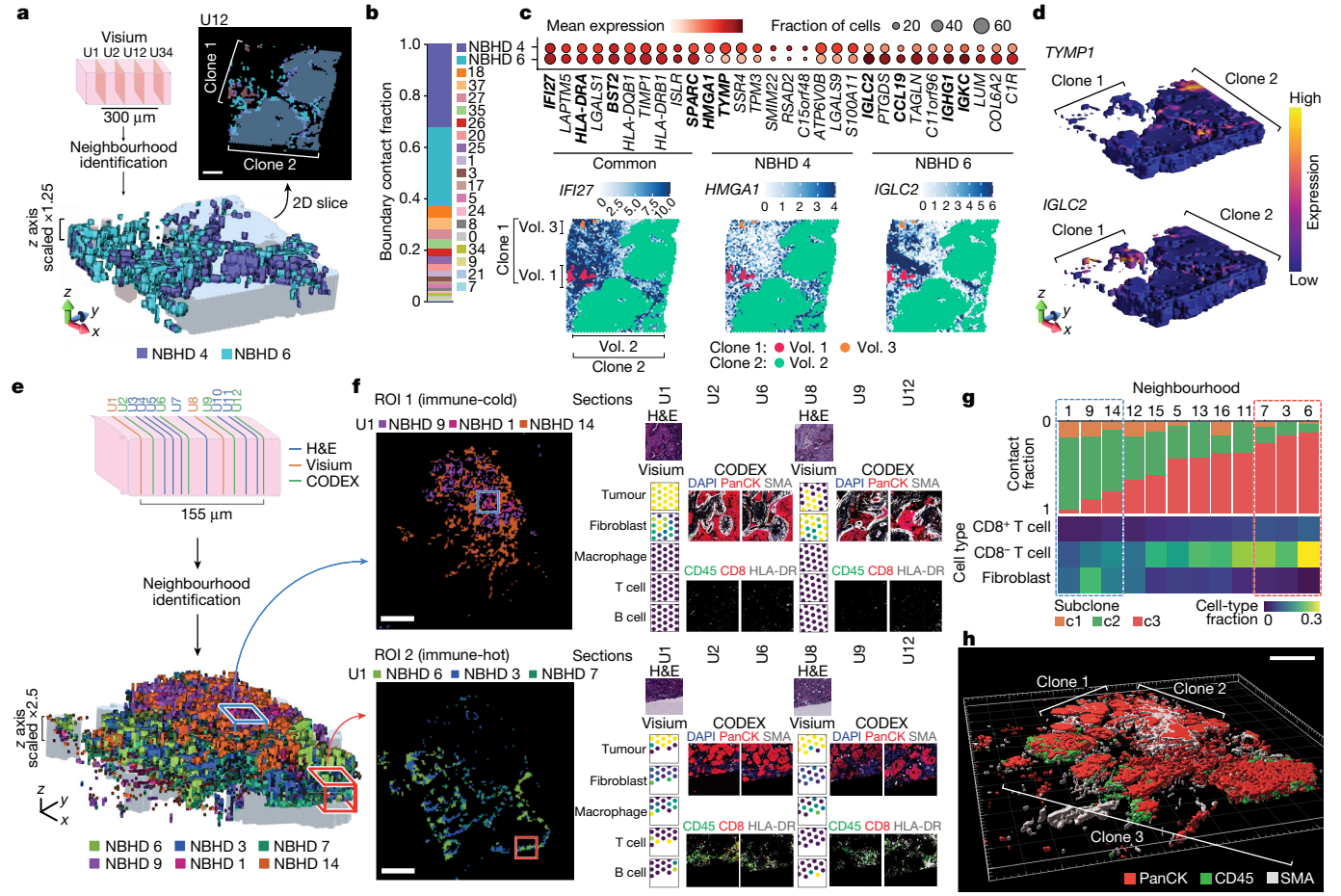

Fig. 5 | Tumour–TME interactions in microregion boundary regions demonstrate heterogeneity. a, For HT268B1, a BRCA metastasis sample, 3D neighbourhood volumes were generated with 4 Visium ST sections spanning 300 µm. Neighbourhoods 4 and 6 (NBHD 4 and NBHD 6, respectively), with the highest contact fraction with the subclone boundary, are displayed in 3D and as a 2D plane overlaid with subclone annotations. Scale bar, 1,000 µm. **b**, TME neighbourhoods displayed by contact fraction with the subclone boundary. **c**, DEGs were categorized into three groups: unique to neighbourhood 4, unique to neighbourhood 6, and shared. Spatial expressions of selected genes from each group are shown (bottom), with genes mentioned in the main text highlighted in bold. **d**, 3D reconstruction of tumour regions, where tumour surface mesh is coloured by the transcript density of *TYMP1* and *IGLC2* within a 50-µm radius of a given location. **e**, For HT397B1, a primary BRCA sample, integrated 3D neighbourhood volumes were generated with 6 H&E, 2 Visium ST and 4 CODEX sections spanning 155 µm. TME neighbourhoods described in **f** are shown as a 3D volume. **f**, Visualization of two ROIs in HT397B1, specifically the more immune-cold ROI 1 and immune-hot ROI 2. 2D slices of the 3D volume with quartile-highlighted neighbourhoods associated with each ROI are shown. Visium ST slides (U1 and U8) are shown as RCTD-imputed cell-type fractions. For CODEX slides (U2, U6, U9 and U12), DAPI, pan-cytokeratin (PanCK), SMA, HLA-DR, CD45 and CD8 are displayed. Scale bar, 500 µm. **g**, TME neighbourhoods are displayed as a fraction of contact with the border of each of the three subclones. Additionally, cell type fraction of $CD8^+$ and $CD8^-$ T cells and fibroblasts are shown. Cell-type fractions were calculated from CODEX sections. The top and bottom quartiles of neighbourhoods with respect to contact fraction with subclone 3 are emphasized as dashed boxes. **h**, 3D epithelial (PanCK, red), immune (CD45, green) and stromal (SMA, white) surface volumes generated from CODEX sections. Scale bar, 500 µm.

transcriptional patterns associated with cancer cell depth from the microregion edge, as well as specific enriched gene expression in edge cells adjacent to immune cells of the TME. Finally, 3D tumour volume reconstruction identified 3D neighbourhoods of regional TME variation.

We observed genomic and transcriptomic heterogeneities among tumour microregions in multiple samples. Although some tumours were relatively consistent in their transcriptomic profiles, others could be subdivided according to gene expression. This variability was partially explained by mapping copy number events to ST regions. Distributions of cancer subclones with genetic variations have been mapped across tissues[40–43], and mutation-based subclones in spatial regions within a single tumour have been demonstrated[15]. In addition to spatial mutation mapping from transcriptome and validation with allele-specific in situ hybridization, we characterized spatial tumour heterogeneity according to changes in gene expression related to the proximity of immune and stromal cell types compared with more insulated cancer cells within spatial microregions. A more nuanced understanding of the way cancer and TME cells shape each other within tumours is needed to better exploit these interactions therapeutically.

Subclonal evolution is a major driver of therapeutic resistance, with the emergence of resistant subclones often resulting in treatment failure[2,3,44]. Here we characterized the structure and distribution of spatially distinct tumour subclones in multiple solid tumours and showed that they can exhibit varying responses to identical compounds through perturbation gene set overlap analysis. Future translational work will probably investigate subclones under the varying selective pressures of anticancer therapies, which will help to guide the design of new approaches, such as optimizing the combination of local and systemic therapies.

There are several limitations of the study. RNA-inferred spatial CNV captures large genetic events but not focal copy number changes. Spatial mutation mappings provide additional support on subclonal identifications, but with the limitation that only mutations near the

3′ end of each transcript are preferentially detected. Additionally, our ST dataset does not achieve single-cell resolution with the current platform (55-µm-diameter spot). Matching snRNA-seq was used to infer tumour–non-tumour expression and CODEX imaging was used to validate our findings on TME composition. However, direct spatial expression from different cell types of origin remains inferred. In closing, our reconstructed 3D data enabled spatial investigation of tumour architecture, subclones, cellular neighbourhoods and TME. We anticipate that such analysis will rapidly establish itself more broadly within cancer research[45]. Coming advancements in technology will facilitate even deeper analyses and will further empower future tumour studies.

Online content

Any methods, additional references, Nature Portfolio reporting summaries, source data, extended data, supplementary information, acknowledgements, peer review information; details of author contributions and competing interests; and statements of data and code availability are available at https://doi.org/10.1038/s41586-024-08087-4.

1. Fu, T. et al. Spatial architecture of the immune microenvironment orchestrates tumor immunity and therapeutic response. *J. Hematol. Oncol.* **14**, 98 (2021).
2. Schmitt, M. W., Loeb, L. A. & Salk, J. J. The influence of subclonal resistance mutations on targeted cancer therapy. *Nat. Rev. Clin. Oncol.* **13**, 335–347 (2016).
3. Roper, N. et al. Clonal evolution and heterogeneity of osimertinib acquired resistance mechanisms in EGFR mutant lung cancer. *Cell Rep. Med.* **1**, 100007 (2020).
4. Trédan, O., Galmarini, C. M., Patel, K. & Tannock, I. F. Drug resistance and the solid tumor microenvironment. *J. Natl Cancer Inst.* **99**, 1441–1454 (2007).
5. Qu, Y. et al. Tumor microenvironment-driven non-cell-autonomous resistance to antineoplastic treatment. *Mol. Cancer* **18**, 69 (2019).
6. Ding, L. et al. Clonal evolution in relapsed acute myeloid leukaemia revealed by whole-genome sequencing. *Nature* **481**, 506–510 (2012).
7. Yang, D. et al. Lineage tracing reveals the phylodynamics, plasticity, and paths of tumor evolution. *Cell* **185**, 1905–1923.e25 (2022).
8. Ståhl, P. L. et al. Visualization and analysis of gene expression in tissue sections by spatial transcriptomics. *Science* **353**, 78–82 (2016).
9. Rao, A., Barkley, D., França, G. S. & Yanai, I. Exploring tissue architecture using spatial transcriptomics. *Nature* **596**, 211–220 (2021).
10. Cui Zhou, D. et al. Spatially restricted drivers and transitional cell populations cooperate with the microenvironment in untreated and chemo-resistant pancreatic cancer. *Nat. Genet.* **54**, 1390–1405 (2022).
11. Black, S. et al. CODEX multiplexed tissue imaging with DNA-conjugated antibodies. *Nat. Protoc.* **16**, 3802–3835 (2021).
12. Greaves, M. & Maley, C. C. Clonal evolution in cancer. *Nature* **481**, 306–313 (2012).
13. Ding, L., Raphael, B. J., Chen, F. & Wendl, M. C. Advances for studying clonal evolution in cancer. *Cancer Lett.* **340**, 212–219 (2013).
14. Erickson, A. et al. Spatially resolved clonal copy number alterations in benign and malignant tissue. *Nature* **608**, 360–367 (2022).
15. Lomakin, A. et al. Spatial genomics maps the structure, nature and evolution of cancer clones. *Nature* **611**, 594–602 (2022).
16. Di Maggio, F. & El-Shakankery, K. H. Desmoplasia and biophysics in pancreatic ductal adenocarcinoma: can we learn from breast cancer? *Pancreas* **49**, 313–325 (2020).
17. Chen, H., Liu, H. & Qing, G. Targeting oncogenic Myc as a strategy for cancer treatment. *Signal. Transduct. Target Ther.* **3**, 5 (2018).
18. Cable, D. M. et al. Robust decomposition of cell type mixtures in spatial transcriptomics. *Nat. Biotechnol.* **40**, 517–526 (2022).
19. Yoshihara, K. et al. Inferring tumour purity and stromal and immune cell admixture from expression data. *Nat. Commun.* **4**, 2612 (2013).
20. Gencheva, R. & Arnér, E. S. J. Thioredoxin reductase inhibition for cancer therapy. *Annu. Rev. Pharmacol. Toxicol.* **62**, 177–196 (2022).
21. Jiang, Y. et al. A systematic analysis of C5ORF46 in gastrointestinal tumors as a potential prognostic and immunological biomarker. *Front. Genet.* **13**, 926943 (2022).
22. Han, L., Li, Z., Jiang, Y., Jiang, Z. & Tang, L. SNHG29 regulates miR-223-3p/CTNND1 axis to promote glioblastoma progression via Wnt/β-catenin signaling pathway. *Cancer Cell Int.* **19**, 345 (2019).
23. Huang, C. K., Sun, Y., Lv, L. & Ping, Y. ENO1 and cancer. *Mol. Ther. Oncolytics* **24**, 288–298 (2022).
24. Zhang, X. et al. Thymosin beta 10 is a key regulator of tumorigenesis and metastasis and a novel serum marker in breast cancer. *Breast Cancer Res* **19**, 15 (2017).
25. Chen, R. H. et al. Tumor cell-secreted ISG15 promotes tumor cell migration and immune suppression by inducing the macrophage M2-like phenotype. *Front. Immunol.* **11**, 594775 (2020).
26. Jin, S. et al. Inference and analysis of cell–cell communication using CellChat. *Nat. Commun.* **12**, 1088 (2021).
27. Filippou, P. S., Karagiannis, G. S. & Constantinidou, A. Midkine (MDK) growth factor: a key player in cancer progression and a promising therapeutic target. *Oncogene* **39**, 2040–2054 (2020).
28. Sick, E. et al. Activation of CD47 receptors causes proliferation of human astrocytoma but not normal astrocytes via an Akt-dependent pathway. *Glia* **59**, 308–319 (2011).
29. Isenberg, J. S., Frazier, W. A. & Roberts, D. D. Thrombospondin-1: a physiological regulator of nitric oxide signaling. *Cell. Mol. Life Sci.* **65**, 728–742 (2008).
30. Jeanne, A. et al. Identification of TAX2 peptide as a new unpredicted anti-cancer agent. *Oncotarget* **6**, 17981–18000 (2015).
31. Wang, Y., Hu, L., Zheng, Y. & Guo, L. HMGA1 in cancer: cancer classification by location. *J. Cell. Mol. Med.* **23**, 2293–2302 (2019).
32. Huang, R., Huang, D., Dai, W. & Yang, F. Overexpression of HMGA1 correlates with the malignant status and prognosis of breast cancer. *Mol. Cell. Biochem.* **404**, 251–257 (2015).
33. Mitselou, A. et al. Predictive role of thymidine phosphorylase expression in patients with colorectal cancer and its association with angiogenesis-related proteins and extracellular matrix components. *In Vivo* **26**, 1057–1067 (2012).
34. Baris, A., Fraile-Bethencourt, E., Eubanks, J., Khou, S. & Anand, S. Thymidine phosphorylase facilitates retinoic acid inducible gene-I induced endothelial dysfunction. *Cell Death Dis.* **14**, 294 (2023).
35. Schmidt, M. et al. Prognostic impact of immunoglobulin kappa C (*IGKC*) in early breast cancer. *Cancers* **13**, 3626 (2021).
36. Wang, J. et al. CCL19 has potential to be a potential prognostic biomarker and a modulator of tumor immune microenvironment (TIME) of breast cancer: a comprehensive analysis based on TCGA database. *Aging* **14**, 4158–4175 (2022).
37. Nishimura, T. et al. Evolutionary histories of breast cancer and related clones. *Nature* **620**, 607–614 (2023).
38. Dang, H. X. et al. The clonal evolution of metastatic colorectal cancer. *Sci. Adv.* **6**, eaay9691 (2020).
39. Simeonov, K. P. et al. Single-cell lineage tracing of metastatic cancer reveals selection of hybrid EMT states. *Cancer Cell* **39**, 1150–1162.e9 (2021).
40. Chen, H. N. et al. Genomic evolution and diverse models of systemic metastases in colorectal cancer. *Gut* **71**, 322–332 (2022).
41. Leung, M. L. et al. Single-cell DNA sequencing reveals a late-dissemination model in metastatic colorectal cancer. *Genome Res.* **27**, 1287–1299 (2017).
42. Hu, Z. et al. Quantitative evidence for early metastatic seeding in colorectal cancer. *Nat. Genet.* **51**, 1113–1122 (2019).
43. Tang, J. et al. Single-cell exome sequencing reveals multiple subclones in metastatic colorectal carcinoma. *Genome Med.* **13**, 148 (2021).
44. Poos, A. M. et al. Resolving therapy resistance mechanisms in multiple myeloma by multiomics subclone analysis. *Blood* **142**, 1633–1646 (2023).
45. Braxton, A. M. et al. 3D genomic mapping reveals multifocality of human pancreatic precancers. *Nature* **629**, 679–687 (2024).

[1]Department of Medicine, Washington University in St Louis, St Louis, MO, USA. [2]McDonnell Genome Institute, Washington University in St Louis, St Louis, MO, USA. [3]Department of Computer Science, Princeton University, Princeton, NJ, USA. [4]Department of Surgery, Washington University in St Louis, St Louis, MO, USA. [5]Siteman Cancer Center, Washington University in St Louis, St Louis, MO, USA. [6]Department of Radiology, Washington University in St Louis, St Louis, MO, USA. [7]Institute for Systems Biology, Seattle, WA, USA. [8]Division of Medical Oncology, Department of Internal Medicine, Washington University School of Medicine, St Louis, MO, USA. [9]Department of Pathology and Immunology, Washington University in St Louis, St Louis, MO, USA. [10]Department of Obstetrics and Gynecology, Washington University in St Louis, St Louis, MO, USA. [11]Division of Urological Surgery, Department of Surgery, Washington University, St Louis, MO, USA. [12]Department of Neuroscience, Washington University School of Medicine, St Louis, MO, USA. [13]Department of Neurosurgery, Washington University School of Medicine, St Louis, MO, USA. [14]Division of Gynecologic Oncology, Department of Obstetrics and Gynecology, Washington University, St Louis, MO, USA. [15]Department of Computer Science and Engineering, Washington University in St Louis, St Louis, MO, USA. [16]Department of Genetics, Washington University in St Louis, St Louis, MO, USA. [17]Department of Otolaryngology–Head and Neck Surgery, Washington University School of Medicine, St Louis, MO, USA. [18]Department of Obstetrics and Gynecology, University of California, San Francisco, San Francisco, CA, USA. [19]These authors contributed equally: Chia-Kuei Mo, Jingxian Liu. [20]These authors jointly supervised this work: Siqi Chen, Erik Storrs, Andre Luiz N. Targino da Costa, Andrew Houston. ✉e-mail: gillandersw@wustl.edu; rcfields@wustl.edu; braphael@princeton.edu; fchen@wustl.edu; lding@wustl.edu

Methods

Experimental methods

Specimens and sample processing. All samples were collected with informed consent at the Washington University School of Medicine in St Louis. Samples from BRCA, PDAC, CRC, CHOL, RCC and UCEC were collected during surgical resection and verified by standard pathology (institutional review board protocols 201108117, 201411135 and 202106166). After verification, a 1.5 × 1.5 × 0.5 cm^3 portion of the tumour was removed, photographed, weighed and measured. Each portion was then subdivided into 6–9 pieces and then further subdivided into 4 transverse-cut pieces. These four pieces were then each respectively placed into formalin, snap-frozen in liquid nitrogen, DMEM and snap-frozen before embedding in OCT. The purpose of choosing grid processing over punch sampling was utility-based, as it minimized remaining tissue. Relevant protocols can be found at protocols.io (https://doi.org/10.17504/protocols.io.bszynf7w)[46].

ST preparation and sequencing. OCT-embedded tissue or FFPE tissue samples were sectioned and placed on a Visium Spatial Gene Expression Slide following the Visium Spatial Protocols–Tissue Preparation guide. Samples used for serial sections were sectioned and collected with an interval range from 5 to 100 µm. When doing serial sectioning, the first section was named as U1, followed by U2, U3, and so on. Selected sections were loaded onto Visium slides and the distance between each section was recorded. For OCT-embedded samples, detailed methods have been described in a previous publication[10]. In brief, fresh tissue samples were coated with room temperature OCT without any bubbles. After RNA quality check using a Tapestation and a morphology check using H&E staining for the OCT-embedded tissue samples, blocks were scored into a suitable size that fit the capture areas and then sectioned into 10-µm sections. Sections were then fixed in methanol, stained with H&E and imaged at ×20 magnification using the bright-field imaging setting on a Leica DMi8 microscope. Tissue samples were then permeabilized for 18 min and ST libraries were constructed following the Visium Spatial Gene Expression Reagent kits user guide CG000239 Rev A (10x Genomics). cDNA was reverse transcribed from the poly-adenylated messenger RNA, which was captured using primers on the slides. Next, the second strand was synthesized and denatured from the first strand. Free cDNA was then transferred from slides to tubes for further amplification and library construction. Libraries were sequenced on a S4 flow cell of an Illumina NovaSeq-6000 system. For FFPE samples, detailed methods have been described in a previous publication[47]. In brief, quality control was done by evaluating DV200 of RNA extracted from FFPE tissue sections per the Qiagen RNeasy FFPE Kit protocol, then followed by performing the Tissue Adhesion Test described in the 10x Genomics protocol. Sections (5 µm) were placed on a Visium Spatial Gene Expression Slide according to the Visium Spatial Protocols–Tissue Preparation guide (10x Genomics, CG000408 Rev A). After overnight drying, slides were incubated at 60 °C for 2 h. Deparaffinization was then performed following the protocol for Visium Spatial for FFPE–Deparaffinization, H&E staining, Imaging and Decrosslinking (10x Genomics, CG000409 Rev A). Sections were stained with H&E and imaged at ×20 magnification using the bright-field imaging setting on a Leica DMi8 microscope. Afterwards, decrosslinking was performed immediately for H&E stained sections. Next, human whole transcriptome probe panels were added to the tissue. After these probe pairs hybridized to their target genes and ligated to one another, the ligation products were released following RNase treatment and permeabilization. The ligated probes were then hybridized to the spatially barcoded oligonucleotides on the capture area. ST libraries were generated from the probes and sequenced on a S4 flow cell of an Illumina NovaSeq 6000 system. Relevant protocols can be found at protocols.io (https://doi.org/10.17504/protocols.io.x54v9d3opg3e/v1 and https://doi.org/10.17504/protocols.io.kxygx95ezg8j/v1)[48,49].

CODEX preparation and imaging. Carrier-free monoclonal or polyclonal anti-human antibodies were purchased (Supplementary Table 3) and verified using immunofluorescence (IF) staining in multiple channels. After screening, antibodies were conjugated using an Akoya Antibody Conjugation kit (Akoya Biosciences, SKU 7000009) with a barcode (Akoya Biosciences) assigned according to the IF staining results. Several common markers were directly purchased through Akoya Biosciences. CODEX staining and imaging were performed according to the manufacturer's instructions (CODEX user manual, Rev C). In brief, 5-µm FFPE sections were placed on coverslips coated with APTES (Sigma, 440140) and baked at 60 °C overnight before deparaffinization. The next day, tissues were incubated in xylene, rehydrated in ethanol and washed in ddH_2O before antigen retrieval with TE buffer, pH 9 (Genemed, 10-0046) in boiling water for 10 min in a rice cooker. The tissue samples were then blocked using blocking buffer (CODEX staining kit, SKU 7000008) and stained with the marker antibody panel to a volume of 200 µl for 3 h at room temperature in a humidified chamber. The dilution factor for each antibody is provided in the CODEX cycle information sheet (Supplementary Table 3). Imaging of the CODEX multicycle experiment was performed using a Keyence fluorescence microscope (model BZ-X810) equipped with a Nikon CFI Plan Apo λ ×20/0.75 objective, a CODEX instrument (Akoya Biosciences) and a CODEX instrument manager (Akoya Biosciences). The raw images were then stitched and processed using the CODEX processor (Akoya Biosciences). After multiplex imaging was completed, H&E staining was performed on the same tissue. Staining quality for each antibody in CODEX is shown as a single channel in green with DAPI in blue in Supplementary Figs. 10 and 11.

Single-nucleus suspension preparation. Approximately 20–30 mg of flash-frozen or cryopulverized or 200 µm of OCT sections of tissue from each sample were retrieved and aliquoted for nucleus preparation for use in a Next GEM Single Cell Multiome ATAC + Gene Expression kit or a Next GEM Single Cell 3′ Kit v.3.1 kit. Samples were resuspended in lysis buffer (10 mM Tris-HCl (pH 7.4) (Thermo, 15567027), 10 mM NaCl (Thermo, AM9759), 3 mM $MgCl_2$ (Thermo, AM9530G), 0.10% NP-40 substitute (% v/v) (Sigma, 74385-1L), 1 mM DTT (Sigma, 646563), 1% stock BSA solution (% v/v) (MACS, 130-091-376), nuclease-free water (Invitrogen, AM9937), plus 0.1 U μl^{-1} RNase inhibitor), resuspended and homogenized through douncing, and filtered through a 40-µm cell strainer (pluriSelect), then diluted with wash buffer (2% BSA, 1× PBS and RNase inhibitor). The filtrate was collected, then centrifuged at 500*g* for 6 min at 4 °C. The nuclear pellet was then resuspended in BSA wash buffer with RNase inhibitor, stained with 7AAD, and nuclei were purified and sorted by FACS. Relevant protocols can be found at protocols.io (https://doi.org/10.17504/protocols.io.14egn7w6zv5d/v1, https://doi.org/10.17504/protocols.io.261gednx7v47/v1)[50,51].

Single-cell suspension preparation. Approximately 15–100 mg of each tumour was cut into small pieces using a blade. Enzymes and reagents from a Human Tumour Dissociation kit (Miltenyi Biotec, 130-095-929) were added to the tumour tissue along with 1.75 ml of DMEM. The resulting suspension was loaded into a gentleMACS C-tube (Miltenyi Biotec, 130-093-237) and subjected to the gentleMACS Octo Dissociator with Heaters (Miltenyi Biotec, 130-096-427). After 30–60 min on the heated dissociation programme (37h_TDK_1), samples were removed from the dissociator and filtered through a 40-µm mini strainer (PluriSelect, no. 43-10040-60) or a 40-µm nylon mesh (Fisher Scientific, 22-363-547) into a 15-ml conical tube on ice. The sample was then spun down at 400*g* for 5 min at 4 °C. After removing the supernatant, when a red pellet was visible, the cell pellet was resuspended using 200 µl to 3 ml ACK lysis solution (Thermo Fisher, A1049201) for 1–5 min. To quench the reaction, 10 ml PBS (Corning; 21-040-CM) with 0.5% BSA (Miltenyi Biotec; 130-091-376) was added and spun down at 400*g* for 5 min at 4 °C. After removing the

supernatant, the cells were resuspended in 1 ml PBS with 0.5% BSA, and live and dead cells were visualized using trypan blue. Finally, the sample was spun down at 400*g* for 5 min at 4 °C and resuspended in 500 µl to 1 ml PBS with 0.5% BSA to a final concentration of 700–1,500 cells per µl. The protocol is available at protocols.io (https://doi.org/10.17504/protocols.io.bsnqnddw)[52].

Single-nucleus library preparation and sequencing. Nuclei and cells and barcoded beads were isolated in oil droplets using a 10x Genomics Chromium instrument. Single-nucleus suspensions were counted and adjusted to a range of 500–1,800 nuclei per µl using a haemocytometer. Reverse transcription was subsequently performed to incorporate cell and transcript-specific barcodes. All snRNA-seq samples were run using a Chromium Next GEM Single Cell 3′ Library and Gel Bead kit v.3.1 (10x Genomics). For the multiome kit, Chromium Next GEM Single Cell Multiome ATAC + Gene Expression was used (10x Genomics). Nuclei were then subjected to downstream protocols by 10x (Next GEM Single Cell Multiome ATAC + Gene Expression: https://cdn.10xgenomics.com/image/upload/v1666737555/support-documents/CG000338_ChromiumNextGEM_Multiome_ATAC_GEX_User_Guide_RevF.pdf. Next GEM Single Cell 3′ Kit v3.1: https://support.10xgenomics.com/single-cell-gene-expression/library-prep/doc/user-guide-chromium-single-cell-3-reagent-kits-user-guide-v31-chemistry-dual-index). Single-cell suspensions were subject to the Next GEM Single Cell 3′ Kit v.3.1 protocol. Barcoded libraries were then pooled and sequenced on an Illumina NovaSeq 6000 system with associated flow cells.

Genomic DNA extraction. Tumour tissue samples were obtained from surgically resected specimens. After a piece was removed for fresh single-cell preparation, the remaining sample was snap-frozen in liquid nitrogen and stored at −80 °C. Before bulk DNA extraction, samples were cryopulverized (Covaris) and aliquoted for bulk extraction. Genomic DNA was extracted from tissue samples with either a DNeasy Blood and Tissue kit (Qiagen, 69504) or a QIAamp DNA Mini kit (Qiagen, 51304). Genomic germline DNA was purified from cryopreserved peripheral blood mononuclear cells using a QIAamp DNA Mini kit (Qiagen, 51304) according to the manufacturer's instructions (Qiagen). The DNA quantity was assessed by fluorometry using a Qubit dsDNA HS assay (Q32854) according to the manufacturer's instructions (Thermo Fisher Scientific). Protocols are available at protocols.io (https://doi.org/10.17504/protocols.io.bsnhndb6)[53].

WES analysis. About 100–250 ng of genomic DNA was fragmented on a Covaris LE220 instrument targeting 250-bp inserts. Automated dual-indexed libraries were constructed using a KAPA Hyper library prep kit (Roche) on a SciClone NGS platform (Perkin Elmer). Up to ten libraries were pooled at an equimolar ratio by mass before the hybrid capture targeting a 5-µg library pool. The library pools were hybridized using xGen Exome Research Panel v.1.0 reagent (IDT Technologies), which spans a 39-Mb target region (19,396 genes) of the human genome. The libraries were hybridized for 16–18 h at 65 °C followed by a stringent wash to remove spuriously hybridized library fragments. Enriched library fragments were eluted and PCR cycle optimization was performed to prevent overamplification. The enriched libraries were amplified using KAPA HiFi master mix (Roche) before sequencing. The concentration of each captured library pool was determined through qPCR using a KAPA library Quantification kit according to the manufacturer's protocol (Roche) to produce cluster counts appropriate for the Illumina NovaSeq-6000 instrument. Next, 2 × 150 paired-end reads were generated targeting 12 Gb of sequence to achieve around 100× coverage per library.

Xenium library preparation and imaging. Paraffin blocks (FFPE blocks) were sectioned at 5 µm and placed on Xenium slides following the FFPE Tissue Preparation guide (10x Genomics, CG000578, Rev B). Those slides underwent a series of xylene and ethanol washes for deparaffinization and decrosslinking, using the FFPE tissue enhancer as outlined (10x Genomics, CG000580, Rev B). Overnight in situ probe hybridization was performed using 379 probes from the Xenium Human Multi-Tissue Panel (10x Genomics, 1000626) plus an additional 100 custom probes (Supplementary Table 6). After hybridization probes were ligated, the sample underwent rolling circle amplification, and the background was quenched using an autofluorescence mixture. Nuclei were stained with DAPI to improve sample tracking and approximate cell boundaries (10x Genomics, CG000582, Rev D). These samples, along with buffers and decoding consumables, were loaded into a Xenium analyzer (10x Genomics, 1000481). The run was initialized using the guidance provided (10x Genomics, CG000584, Rev C). These fluorescent reporters hybridized to targeted complementary regions of the barcoded circularized cDNA were imaged. H&E staining was performed on the same region after the run was complete.

Analytical methods

Quantification and statistical analysis. All data analyses were conducted in R and Python environments. Details of specific functions and libraries are provided in the relevant methods sections above. Significance was determined using the Wilcoxon rank-sum test, proportion test, hypergeometric test or Pearson correlation test, as appropriate. P values < 0.05 were considered significant. Details of statistical tests are provided in the figure legends and the relevant methods sections.

WES data processing. FASTQ files were preprocessed using trimGalore (v.0.6.7; with parameters: --length 36 and all other parameters set to default; https://github.com/FelixKrueger/TrimGalore). FASTQ files were then aligned to the GDC's GRCh38 human reference genome (GRCh38.d1.vd1) using BWA-mem (v.0.7.17) with parameter -M and all others set to default. The output SAM file was converted to a BAM file using the samtools (https://github.com/samtools/samtools; v.1.14) view with parameters -Shb, and all others set to default. BAM files were sorted and duplicates were marked using Picard (v.2.6.26) SortSam tool with the following parameters: CREATE_INDEX=true, SORT_ORDER=coordinate, VALIDATION_STRINGENCY=STRICT, and all others set to default; and MarkDuplicates with parameter REMOVE_DUPLICATES=true, and all others set to default. The final BAM files were then indexed using the samtools (v.1.14) index with all parameters set to default.

Mutation calling using WES. Somatic mutations were called from WES data using the Somaticwrapper pipeline (v.2.2; https://github.com/ding-lab/somaticwrapper), which includes four different callers: Strelka (v.2.9.10)[54], MUTECT (v.1.1.7)[55], VarScan (v.2.3.8)[56] and Pindel (v.0.2.5)[57]. We kept exonic single nucleotide variants (SNVs) called by any two callers among MUTECT (v.1.1.7), VarScan (v.2.3.8) and Strelka (v.2.9.10) and insertions and deletions (indels) called by any two callers among VarScan (v.2.3.8), Strelka (v.2.9.10) and Pindel (v.0.2.5). For the merged SNVs and indels, we applied a 14× and 8× minimal coverage cut-off for tumour and normal tissue, respectively. We also filtered SNVs and indels by a minimal VAF of 0.05 in tumours and a maximal VAF of 0.02 in normal samples. We also filtered any SNV within 10 bp of an indel found in the same tumour sample. Finally, we rescued the rare mutations with VAFs within 0.015 and 0.05 based on an established gene consensus list[58,59]. In a downstream step, we used Somaticwrapper to combine adjacent SNVs into double-nucleotide polymorphisms using COCOON (https://github.com/ding-lab/COCOONS), as reported in a previous study[60].

Mutation mapping to snRNA-seq and ST data. We applied an in-house tool called scVarScan that can identify reads supporting the reference allele and variant allele covering the variant site in each cell by tracing cell and molecular barcode information in a snRNA-seq and

single-cell RNA sequencing (scRNA-seq) or Visium bam file. The tool is freely available at GitHub (https://github.com/ding-lab/10Xmapping). For mapping, we used high-confidence somatic mutations from WES data produced by Somaticwrapper (described above). Visium reads were prefiltered with the flag 'xf:i:25' for reads contributing to unique molecular identifier counts.

Spatial mutation VAF statistical test. For each ST section, we applied two sets of statistical tests to all WES-based somatic mutations mapped to ST. First, for each mutation with greater than 30 reads of coverage on ST across all spots, the VAF was calculated for all tumour region spots and all non-tumour region spots as the number of variant reads across all spots divided by the number of total reads across all spots. A binomial test was then done using VAF of non-tumour spots as the background: binom.test(alterative="greater"). Then, a proportion test was done between the VAFs in different spatial subclones with prop. test(alternative="two.sided"). Finally, multiple testing correction was done on both sets of tests with the function p.adjust().

CNV calling using WES. Somatic CNVs were called using GATK (v.4.1.9.0)[61]. Specifically, the hg38 human reference genome (NCI GDC data portal) was binned into target intervals using the PreprocessIntervals function, with the bin length set to 1,000 bp and using the interval-merging-rule of OVERLAPPING_ONLY. A panel of normals was then generated using each normal sample as input and the GATK functions CollectReadCounts with the argument --interval-merging-rule OVERLAPPING_ONLY, followed by CreateReadCountPanelOfNormals with the argument --minimum-interval-median-percentile 5.0. For tumour samples, reads that overlapped the target interval were counted using the GATK function CollectReadCounts. Tumour read counts were then standardized and denoised using the GATK function DenoiseReadCounts, with the panel of normals specified by --count-panel-of-normals. Allelic counts for tumours were generated for variants present in the af-only-gnomad.hg38.vcf according to GATK best practices (variants further filtered to 0.2 > af > 0.01 and entries marked with 'PASS') using the GATK function CollectAllelicCounts. Segments were then modelled using the GATK function ModelSegments, with the denoised copy ratio and tumour allelic counts used as inputs. Copy ratios for segments were then called on the segment regions using the GATK function CallCopyRatioSegments.

Bedtools[62] intersection was used to map copy number ratios from segments to genes and to assign the called amplifications or deletions. For genes overlapping multiple segments, a custom Python script was used to call that gene as amplified, neutral or deleted based on a weighted copy number ratio calculated from the copy ratios of each overlapped segment, the lengths of the overlaps and the *z* score threshold used by the CallCopyRatioSegments function. If the resulting *z* score cut-off value was within the range of the default *z* score thresholds used by CallCopyRatioSegments (v.0.9,1.1), then the bounds of the default *z* score threshold were used instead (replicating the logic of the CallCopyRatioSegments function).

ST data processing. For each sample, we obtained the unfiltered feature–barcode matrix per sample by passing the demultiplexed FASTQ files and associated H&E image to Space Ranger (v.1.3.0, v.2.0.0 and v2.1.0 'count' command using default parameters with reorient-images enabled) and the prebuilt GRCh38 genome reference 2020-A (GRCh38 and Ensembl 98). Seurat was used for all subsequent analyses. We constructed a Seurat object using the Load10X_Spatial function for every slide. Each slide was then scaled and normalized with the SCTransform function to correct for batch effects. Any merged analysis or subsequent subsetting of cells and samples for a sample with several slides underwent the same scaling and normalization method. Spots were clustered using the original Louvain algorithm, and the top 30 principal component analysis dimensions using the FindNeighbors and FindClusters functions as described in the 'Analysis, visualization, and integration of spatial datasets with Seurat' vignette from Seurat (https://satijalab.org/seurat/articles/spatial_vignette.html).

InferCNV and CalicoST for CNV calling on Visium ST data. To detect large-scale chromosomal CNVs using scRNA-seq, snRNA-seq and Visium data, InferCNV (v.1.10.1) was used with default parameters recommended for 10x Genomics data (https://github.com/broad-institute/inferCNV). InferCNV was run at the sample level and only with post-quality control filtered data using the raw counts matrix. For snRNA-seq and scRNA-seq data, all non-malignant cells were used as a reference with the annotation 'non-tumour' and all malignant cells had the same annotation 'tumour', with the following parameters: analysis_mode="subclusters", --cluster_by_groups=T, --denoise=T, and --HMM=T. For Visium ST data, 200 spots annotated as 'non-malignant' with the lowest ESTIMATE purity score were used as a reference, and 'malignant' spots had their microregion ID as annotation, with the following parameters: window_length=151, analysis_mode="sample", --cluster_by_groups=T, --denoise=T, and --HMM=T. CalicoST (https://github.com/raphael-group/CalicoST)[63] was run on Visium ST data with the same input annotation (microregion ID). All spots from the same microregions were treated as the smallest unit of analysis. CalicoST was then run with default parameters with results manually inspected.

Copy number profile similarity score calculation. To determine the similarity between two spatial CNV profiles, we use a modified Jaccard similarity score. A CNV profile was defined as a set of genomic windows with annotation copy number neutral (0), amplification (1) or deletion (−1). Two CNV profiles were then compared, and overlapping genomic windows were broken down so that both profiles had the same sets of windows (with the function reduced from the package GenomicRanges v.1.46.1). Then, the CNV similarity score (Sim) was defined as follows:

$$\mathrm{Sim}_{A,B} = \frac{\sum_i \mathrm{size}(w_i) \times (\mathrm{CNV}_{A,i} \times \mathrm{CNV}_{B,i})}{\sum_i \mathrm{size}(w_i)}$$

where w_i denotes the size of the genomic window i, $\mathrm{CNV}_{A,i}$ denotes the CNV annotation (0, 1 or −1) for profile A in genomic window i, and $\mathrm{CNV}_{B,i}$ denotes the CNV annotation for profile B in genomic window i across all genomic windows where either A or B is not CNV neutral.

To determine the similarity between a spatial CNV profile and WES-based CNV (related to Extended Data Fig. 5a), we used a similarity score averaging the sensitivity (fraction of WES-based CNVs also detected in spatial CNVs) and specificity (fraction of spatial CNVs agreeing with WES-based CNVs). Specifically,

$$\mathrm{Sim}_{A,E} = \left(\frac{\sum_a w_a \times (\mathrm{CNV}_{A,a} \times \mathrm{CNV}_{E,a})}{\sum_a w_a} + \frac{\sum_e w_e \times (\mathrm{CNV}_{A,e} \times \mathrm{CNV}_{E,e})}{\sum_e w_e} \right) / 2$$

where w_a denotes the size of the genomic window a from spatial CNV, w_e denotes the size of the genomic window e from a WES-based CNV, $CNV_{A,a}$ denotes the CNV annotation (0, 1 or −1) for profile A in genomic window a.

Spatial subclone identification based on CNV profile similarity. In the OCT workflow (Supplementary Fig. 1a), CalicoST simultaneously identified CNVs and groups microregions into spatial subclones. In the FFPE workflow, confident spatial CNV events in each microregion were first selected by comparing them with matching WES. Then, a pairwise CNV similarity score was calculated across all tumour microregions. Finally, microregions were clustered with CNV similarity scores using the function hclust (d = 1-CNV similarity, method="ward.D2"), and divided into clusters with function cutree (h = 0.8 × max(hclust$height)). Final subclone assignments were manually reviewed to avoid overclustering and to eliminate small outlier CNV profiles.

Tumour microregion annotation and layer determination. Using Visium ST, tumour microregions were determined through a multi-step process using H&E. Each ST spot was assigned as either stroma or tumour by manually reviewing the morphology on H&E stained sections. If at least 50% of the pixels within a spot covered malignant cell morphology, the spot was labelled as tumour. Otherwise, it was labelled as stroma. Next, we defined distinct tumour microregions using a set of three rules. The first rule specified that tumour spots immediately adjacent to one another are initially marked as a single tumour microregion. The second rule states that if two distinct tumour regions together occupied at least 50% of one single spot, the spot is assigned to the distinct tumour region with the higher percentage occupied. Finally, the third rule specified that if there was a clear morphological difference of the tumour spots within one tumour microregion, the microregion must be separated into distinct microregions, one per clear morphology.

Afterwards, we ran the Morph toolset (https://github.com/ding-lab/morph), which uses mathematical morphology to refine the tumour microregions. That is, if the total number of spots in a microregion is less than or equal to three, then we labelled all such spots as stroma. Last, Morph assigned the layer (for example, T1) of each spot of a tumour microregion by a sequence of mathematical morphology operations described in the Spot-depth correlation analysis method, which denotes the depth of a given spot inside a microregion.

Average spot area and microregion size calculation. To calculate the area each spot takes, we used the spot size (55 μm) and centre-to-centre distance between each spot (100 μm) provided by 10x Genomics (http://kb.10xgenomics.com/hc/en-us/articles/360035487572-What-is-the-spatial-resolution-and-configuration-of-the-capture-area-of-the-Visium-v1-Gene-Expression-Slide-). As illustrated in Supplementary Fig. 6, the Visium spots form a hexagonal lattice that covers the sample. The repeating unit of this lattice is a trapezoid shape centred at each spot's centre that is composed of eight equilateral triangles. Each triangle has a side of 50 μm (half of the spot the centre-to-centre distance). Using the area equation of equilateral triangles and multiplying it by 8, we obtained the area of each trapezoid as 8,660 μm^2, which is the average area occupied by each spot. To calculate the microregion size, we multiplied the spot count by 8,660 and divided by 10^6 to obtain the size in mm^2.

Micoregion density estimation. We estimated microregion density per section by following the formula: density per μm^2 = *n* microregion per section size (in spots) then divided by 8,660 μm per spot. Then density per mm^2 = density per $\mu m^2 \times 10^6$ (*n* microregion per mm^2).

Cell-type annotation. Cell-type assignment was done based on the following known markers: B cell, *CD79A*, *CD79B*, *CD19*, *MS4A1*, *IGHD*, *CD22* and *CD52*; cDC1, *CADM1*, *XCR1*, *CLEC9A*, *RAB32* and *C1orf54*; cDC2, *CD1C*, *FCER1A*, *CLEC10A* and *CD1E*; mregDC, *LAMP3*, *CCR7*, *FSCN1*, *CD83* and *CCL22*; pDC, *IL3RA*, *BCL11A*, *CLEC4C* and *NRP1*; macrophage, *CX3CR1*, *CD80*, *CD86*, *CD163* and *MSR1*; mast cell, *HPGD*, *TPSB2*, *HDC*, *SLC18A2*, *CPA3* and *SLC8A3*; endothelial, *EMCN*, *FLT1*, *PECAM1*, *VWF*, *PTPRB*, *ACTA2* and *ANGPT2*; fibroblast, *COL1A1*, *COL3A1*, *COL5A1*, *LUM* and *MMP2*; pericyte, *RGS5*, *PLXDC1*, *FN1* and *MCAM*; NK cell, *FCGR3A*, *GZMA* and *NCAM1*; plasma cell, *CD38*, *SDC1*, *IGHG1*, *IGKC* and *MZB1*; T cell, *IL7R*, *CD4*, *CD8A*, *CD8B*, *CD3G*, *CD3D* and *CD3E*; and regulatory T cell, *IL2RA*, *CTLA4*, *FOXP3*, *TNFRSF18* and *IKZF2*. Normal epithelial cells in the breast were annotated with the following markers: LumSec, *GABRP*, *ELF5*, *CL28*, *KRT15*, *BARX2* and *HS3ST4*; LumHR, *ANKRD30A*, *ERBB4*, *AFF3*, *TTC6*, *ESR1*, *NEK10* and *XBP1*; and basal, *SAMD5*, *FBXO32*, *TP63*, *RBBP8* and *KLHL13*. Normal epithelial cells in the liver were annotated with the following markers: hepatocyte, *ALB*, *CYP3A7*, *HMGCS1*, *ACSS2* and *AKR1C1*; cholangiocyte, *SOX9*, *CFTR* and *PKD2*. Normal epithelial cells in the pancreas, including ductal, acinar, islet-α, islet-β and islet-γ cells, were annotated with singleR (v.1.8.1) using reference data BaronPancreasData('human').

Spot-depth correlation analysis. We identified a correlation between gene expression and spot depth in its tumour microregion. First, each spot was assigned a depth defined as the distance to the closest TME-facing spot in its tumour microregion. This depth was quantified in several layers through an iterative process whereby all the malignant spots immediately adjacent to non-malignant spots were considered layer 1, and then all malignant spots immediately adjacent to layer 1 were considered layer 2, and the process was repeated until all spots were assigned with a layer number. If a spot's layer was larger than the smallest distance between the spot and any Visium border (including the edge of the Visium capture window, edge of the tissue section and any empty spots inside the section), then we excluded such spots, as we only knew the upper bound of the depth of this spot. Additionally, tumour microregions with fewer than 3 layers or 50 spots were excluded from the analysis. The distance between layers was taken as the centre-to-centre distance of Visium spots (100 μm).

To give the same weight to bigger and smaller regions, the depth of each spot was further normalized by the maximum depth of the microregion this spot belonged. Then, we performed partial correlation tests independently between gene expression (at least 1 transcript detected from the gene in more than 50% of all spots) and normalized depth of each spot, with tumour purity as a covariate as follows:

$$\text{Expression} = \text{rho} \times (\text{layer fraction}) + b \times \text{purity}$$

where layer fraction is the layer number divided by the total number of layers in a tumour to normalize for large and small microregions, rho is the layer correlation coefficient, and *b* is the correlation coefficient for covariant purity. Purity was inferred with deconvolution when there was matching snRNA-seq data (deconvoluted tumour fraction per spot by RCTD), or with ESTIMATE (that is, tumour purity estimate score per spot) otherwise. Each gene was checked against a set of snRNA-seq-derived non-malignant gene lists to ensure that the change in fraction did not derive from a shift in cell type composition. Finally, we performed multiple-testing adjustments for all tests done in each ST section.

Spot-depth GSEA pathway enrichment analysis. To summarize biological programs enriched in the centre and periphery of tumour microregions across sections, we first obtained the cohort-level average layer correlation coefficient. If a test was not significant ($P \geq 0.05$), rho was assigned to be 0 to indicate no correlation. If a test was not performed on a section (<50% of the spots have at least one transcript), rho was also assigned as 0. When a case had multiple sections, we first took the average rho across sections to avoid bias towards tumours with more sections. Then, the average of rho was calculated for each cohort (all samples or samples from each cancer type).

In the same fashion, rank statistics were calculated for each test as $-\log_{10}(P \text{ value}) \times \text{rho}$ for tests with $P < 0.05$. For tests with $P \geq 0.05$ or genes not tested, the rank statistic was 0. We then calculated average rank statistics per case, followed by the average per cancer type. Finally, with the full list of rank statistics calculated for all genes tested, we used the function GSEA (parameters: pvalueCutoff=0.5; package: clusterProfiler v.3.18.1) to obtain the normalized enrichment score of Hallmark pathways (package: msigdbr 7.5.1) from the MSigDB[64]. Finally, only pathways with $P < 0.1$ were kept in the final results.

Tumour intrinsic and non-tumour gene categorization. We use differential expression and per cent expression filters, comparing expression among cell types in the matching snRNA-seq data to further characterize genes identified in the centre and periphery enriched analysis. The steps implemented in this workflow generated four

categories: tumour-specific, stromal-specific, tumour-enriched and stromal-enriched (Supplementary Fig. 8a,b). Genes that did not pass the significant cutoff in any differential expression analysis were labelled separately as not DEG.

To distinguish these four groups, we first performed differential gene analysis of cell types in the matching snRNA-seq data, filtered by a conventional significance cut-off ($\log_2$(fold change) > 0.5, adjusted $P < 0.05$, Bonferroni correction), to obtain DEGs (Supplementary Fig. 8a). Given the heterogeneity in tumours, certain tumour-specific genes might only exist in a subpopulation of tumours. Therefore, we first subclustered the tumour populations (using the Subcluster function in Seurat with a resolution of 0.5) to obtain tumour subclusters. We then compared each subcluster with all other non-tumour cells. A gene was considered a tumour DEG if at least one tumour subcluster showed significant expression compared with the non-tumour cells and vice versa for non-tumour DEGs (Supplementary Fig. 8a,b).

For candidate tumour or stromal-specific genes, a DEG was designated as tumour-specific if it met both of the following criteria: (1) it is a DEG when compared with all non-tumour cell types from at least one tumour subcluster; and (2) its expression was <15% in all non-tumour cell types (Supplementary Fig. 8c).

The reverse applied to candidate stromal-specific DEGs. If a DEG did not meet both of these requirements to be tumour or stromal specific, it was designated as either tumour-enriched or stromal-enriched based on whether the expression level was higher in tumour or stromal cell types (Supplementary Fig. 8a).

Spatial subclone-specific treatment response analysis. We focused on ten cases (comprising four BRCA, two CRC and four PDAC samples) with multiple spatial subclones for this analysis. To obtain subclone-specific DEGs, we used FindMarkers from the function in Seurat with the 'wilcox' test option DEGs between each subclone and TME. We then applied the cut-off for adjusted $P < 0.01$, average $\log_2$(fold change) > 1 and per cent expression in at least one cell type > 0.4 to select significant DEGs. To infer treatment response, we used the perturbation database LINCS L1000 (ref. 65), specifically the LINCS_L1000_Chem_Pert_down dataset from Enrichr[66], to evaluate the gene set overlap between upregulated DEGs in spatial subclones and downregulated genes after compound treatment. To make the plot in Supplementary Fig. 4, we sorted the data by 'Odd.Ratio' and selected top compounds from each subclone. The corresponding compound metadata, including mechanism of action, was obtained from CLUE (clue.io, 'Expanded CMap LINCS Resource 2020 Release') to add annotation on the heatmap.

Organ-specific gene blacklist for non-malignant cell types. To distinguish transcripts originating from cancerous versus non-malignant stromal or immune cells, we used merged snRNA-seq data per organ (breast, kidney, liver and pancreas) for cell-type marker analysis. This analysis used the FindAllMarkers function in Seurat with the 'wilcox' test option. Subsequently, we refined the gene list by applying filters such as average $\log_2$(fold change) > 2, per cent expression in at least one cell type > 0.4 and adjusted P values < 0.01 to ensure robust marker selection for each cell type. The resultant gene list is available in Supplementary Table 5. This list was instrumental in excluding non-cancerous cell genes from analyses pertaining to cancer-specific expression patterns, such as pairwise microregion similarity analysis. Of note, during the analysis, we observed a notable mapping of various epithelial cell types in the snRNA-seq reference dataset for BRCA when using the RCTD deconvolution method. This observation probably stems from the diverse BRCA subtypes present in the cohort. To address this, we opted to combine all epithelial cell types into a single category during the identification of cell-type markers and excluded them from the blacklist. For tumours originating from organs other than the four mentioned above, we aggregated all genes present in the blacklist across organs to form a comprehensive multiorgan blacklist, which aided in filtering out non-cancerous transcripts.

Microregion transcriptional profile analysis. For overall tumour heterogeneity, we selected Morph-identified spots then ran ROGUE (v.1.0)[67] to measure heterogeneity as 1-ROGUE. We then compared the transcriptional profiles of microregions by selecting the top 500 most variable features after excluding stroma regions in ST samples following Morph processing. Our initial evaluation involved conducting Pearson correlation tests for each pair of microregions, using a range of the top 250–1,500 most variable genes with increments of 250 (that is, 250, 500, 750, …, 1,500). We observed consistent correlations for nearly all values beyond using more than 500, which led us to select the top 500 genes for this analysis. This choice reduced the risk of selecting too few variable genes (for example, <250 most variable genes) while also avoiding the inclusion of numerous genes with minimal effect on the transcriptional profile. GSEA analysis was done using the function GSEA (parameters: pvalueCutoff = 0.5; package: clusterProfiler v.3.18.1) to obtain the normalized enrichment score of Hallmark pathways (package: msigdbr v.7.5.1) from the MSigDB[64].

Module score calculation. Module scores on top of each heatmap in Extended Data Fig. 6 were calculated with the AddModuleScore function from Seurat[68] using the genes listed in each heatmap. This score represents the average expression levels of a gene set. The score was calculated for each spot and a box plot was used to show the distribution of module scores in each microregion.

ST cell-type decomposition. Cell-type composition per spot was deconvolved using RCTD[18] with default parameters and doublet_mode = 'multi'. The reference for each run was the cell types manually annotated from the Seurat object of the matching snRNA-seq or Multiome sample. To quantify spatial distribution of each cell type, cell type fraction of 6 layers (T3 and above, T2, T1, E1, E2, E3 and above) from each tumour microregion is calculated and averaged in each sample. To compare differential TME infiltration between spatial subclones, cell type fraction from all spots between spatial subclones was compared with pairwise Wilcoxon rank-sum test and FDR adjustment.

Spatial cell–cell interaction at tumour boundary. We evaluated the spatial-based cell–cell interaction (CCI) in the ST sample using COMMOT[69] with CellChat database and distance threshold of 1,000 μm, following the same threshold used in the original publication for Visium. The median sender and receiver signals for each interaction family were compared between all tumour boundary spots (including tumour boundary layer and TME boundary layer) and all non-boundary spots (Wilcoxon rank-sum test) on a sample. Interaction pathways with signal difference great than 0.1 and FDR less than 0.05 are considered significantly boundary-enriched. Boundary DEGs were identified with FindMarkers function on three sets of comparisons: boundary/tumour, boundary/TME and boundary/all non-boundary. A boundary DEG has adjusted P value 0.25 in boundary/non-boundary test, and $\log_2$(fold change) > 0 in the other two tests.

Serial section alignment and branching factor calculation. We applied PASTE2 (ref. 70), the updated ST-based alignment tool PASTE[70], to enable partial image alignment. Serial sections of the same tumour piece were aligned pairwise with default settings. Each Visium data point in every ST section received new coordinates, denoted as x' and y', based on the alignment results. We then identified the nearest spot on each adjacent section for every spot, connecting them along the z axis. This process facilitated the linking of spots across all sections on the z axis. To assess whether one microregion was connected to another in an adjacent section, we first removed stromal spots and then counted the connected spots. If any microregion on one section connected to

the next section with more than three shared spots, then we considered these two microregions, located on different sections, as connected in 3D space and forming the same tumour volume. This connection was labelled as volume 1, volume 2, and so forth in the figures (Fig. 5d,e and Extended Data Fig. 9a–d).

We used two geometric metrics to describe tumour volume: connectivity and loop. For connectivity (degree), this metric quantifies the number of connections from an individual microregion to adjacent sections. For example, if microregion 2 in section 2 connects to 3 microregions in section 1 and 2 in section 3, its connectivity is 5. The maximum connectivity of a tumour volume is the highest connectivity among its microregions. For loop, this metric was calculated as the total number of connections minus the total number of microregions plus one, identifying intricate loop structures within the tumour volume.

Registration of Visium, CODEX and H&E serial sections. Before registration, imaging data underwent the following transformations. Multiplex images were converted to greyscale images of DAPI intensity. The image was then downscaled by a factor of 5 before key point selection. H&E images (also downsampled by a factor of 5) were used for keypoint selection with Visium data.

For registration, we used BigWarp[71], which was packaged in the Fiji/ImageJ software application. To register each collection of serial images, we used the first serial section as the fixed image and the second image as the moving image. After the second image was warped to the first image, the second image was used as the fixed image for the transformation of the third image. Key point registration proceeded in this fashion for all images in the serial section experiment. A total of 4–20 key points were selected per image transformation. Once key points were selected, a moving field was exported from BigWarp for each image transformation. This dense displacement field was then upscaled by a factor of 5 so it could be used to warp the full-resolution imaging data. The full-resolution dense displacement field was then used to register its corresponding multiplex or Visium data. The code used for registration is available at GitHub (https://github.com/ding-lab/mushroom/tree/subclone_submission).

Neighbourhood identification input preprocessing. Once imaging data were registered, they were processed in the following manner before model input.

For Visium ST data, genes were limited to genes expressed in a minimum of 5% of spots across all serial sections and expression counts were $\log_2$ transformed. CODEX, Visium ST and H&E data were normalized by subtracting the mean expression and dividing by the standard deviation for each gene.

Expression profiles for each patch were generated differently for image-native data (CODEX and H&E) and point-based data (Visium). Expressions for CODEX and H&E patches were calculated as the average pixel intensities for each image channel over all pixels within the patch bounds. Visium patches were calculated in largely the same manner; however, the expression profile of each spot within the patch was linearly weighted by its distance to the centre of the patch. This differential weight helped to account for variation expression due to the number of spots that fall within patch boundaries.

Neighbourhood identification model architecture. The neighbourhood annotation model consisted of an autoencoder with a vision transformer (ViT) backbone (Supplementary Fig. 7). In brief, an autoencoder is an unsupervised training method for which an encoder (embedding component) and a decoder (reconstruction component) work together to learn how input data are generated. Specifically, the network derives an approximation, Q, to the true posterior generating function, P, for the output, given the input. The autoencoder used was asymmetric, meaning that the encoder and decoder were not inverse copies of one another. The encoder consisted of a ViT with a similar architecture to previously described architectures[72,73] (Supplementary Table 4).

ViTs work on image tokens as input. In brief, image tokens are n-dimensional representations of patches of the input image. During training, image tiles were sampled from a uniform distribution across the set of input sections (Supplementary Fig. 7a). The sampled tile was then split into patches, for which the number of patches was determined by two hyperparameters: patch height (ph) and patch width (pw). Each patch was then flattened to a $1 \times (\text{ph} \times \text{pw} \times c)$ vector, where c is the number of channels in the image (in the case of spatial transcriptomics data, c is the number of genes). The unrolled patches were then concatenated into a $n \times (\text{ph} \times \text{pw} \times c)$ matrix, where n is the number of patches in the image tile. Each row in this matrix is a token that represents a patch in the image tile. The tokens were then projected by a linear layer to shape $n \times d$, where d is the dimension of the transformer blocks.

After this, a slide token was concatenated to patch tokens. The slide token (representing the slide from which the image tile was selected) was indexed from a trainable embedding of size $n\_\text{slides} \times d$, where n_slides is the number of slides in the serial section experiment. The motivation for the slide token is that as it is passed through the transformer blocks, along with the patch tokens, information can be shared across all tokens, allowing the slide token to learn to attend to useful representations of the patches. This feature allowed the model to be more robust to batch effects between serial sections. Following the addition of the slide token, positional embeddings were added to all tokens and passed through the transformer blocks comprising the ViT encoder. All variables above and details of the transformer architecture are available in Supplementary Table 4.

Once passed through the encoder, patches were represented as an embedding of size $n \times d$. The next step of the architecture was neighbourhood assignment. Neighbourhoods were assigned to patches in a hierarchical manner, meaning that a patch was classified into several neighbourhoods that differed in level of specificity. For each level of the neighbourhood hierarchy, the subsequent levels comprised partitions of the previous levels' neighbourhoods, that is, except for the first level, each neighbourhood was a subset of a neighbourhood in a previous level of the hierarchy. For this analysis, the model generated three levels of neighbourhoods, each with the capacity to discover up to $n = 8$ (level 1), $n = 32$ (level 2) and $n = 64$ (level 3) neighbourhoods, respectively. For this analysis, all neighbourhoods shown are neighbourhoods annotated at hierarchy level 3. The model contained three codebooks (one for each level) that are of size $n\_\text{NBHDs} \times d$, where n_NBHDs is the number of possible neighbourhoods that can be assigned for the given level. The patch embeddings output by the ViT encoder were projected by three independent blocks of linear layers (one for each level) that output each patch's probability of assignment to a given neighbourhood. These probabilities were then used to retrieve neighbourhood embeddings from the codebook corresponding to the neighbourhood level. Three linear blocks (one for each level) were then used to independently reconstruct patch embeddings at each level to each patch's original pixel values. The code used for training the model is available at GitHub (https://github.com/ding-lab/mushroom/tree/subclone_submission).

Model loss function. The overall loss function has two main contributions: mean squared error (MSE) on the reconstruction of the input patches, and cross-entropy loss on the encoded distribution and the normal distribution with 0 mean and 1.0 variance.

During training, the autoencoder was simultaneously trying to optimize two main tasks: the reconstruction of the expression profile of each image patch embedding and the alignment of neighbourhood labels between adjacent sections. These two competing objectives forced the model to learn representative expression patterns while also keeping neighbourhoods aligned between input sections, which helped

to combat neighbourhood differences due to batch effects. Differences in patch expression were quantified by MSE, whereas neighbourhood adjacency was enforced by minimizing the cross-entropy of patches adjacent to each other in the z direction during training.

The overall loss function is defined below:

$$\mathbf{L}_{\text{overall}} = \lambda_{\text{NBHD}}\mathbf{L}_{\text{NBHD}} + \lambda_{\text{MSE}}\mathbf{L}_{\text{MSE}}$$

Where λ_{NBHD} (maximum of 0.01) and λ_{MSE} (set to 1.0) are scalers for the neighbourhood loss ($\mathbf{L}_{\text{NBHD}}$) and reconstruction loss ($\mathbf{L}_{\text{MSE}}$), respectively. During training, λ_{NBHD} for was linearly increased from 0 to its maximum value.

Model training and inference. Two separate runs of the model were trained for HT397B1 (six H&E, four CODEX and two Visium ST slides) and HT268B1 (four Visium ST slides). Training hyperparameters, such as batch size and number of training steps, are provided in Supplementary Table 4. For HT268B1, only one instance was trained because only one data type was present. For HT397B1, three model instances were trained (one for each data type) and were subsequently merged following the procedure described in the section '3D neighbourhood construction and integration'.

Following training, the model inference was performed on overlapping image tiles for each slide using a sliding window of size 8 and a stride of 2 (that is, 2 overlapping patches between image tiles). The 2 × 2 centre patches of each tile were extracted and retiled to match the original slide orientation. Each reconstructed 'patch embedding image' was at a resolution of 50 pixels μm^{-1} (that is, each neighbourhood patch represents an area that is 50 μm wide) with the exception of Visium ST, for which the patch resolution was 100 pixels μm^{-1}.

3D neighbourhood construction and integration. After the assignment of neighbourhoods for each section, slides were interpolated to generate a 3D neighbourhood volume. For this, we used linear interpolation of neighbourhood assignment probabilities with the torchio library[74].

Following interpolation, we also integrated neighbourhood volumes for HT397B1, for which multiple data-type-specific volumes were generated using a graph-based clustering approach. In brief, all overlapping neighbourhood voxel annotations were identified. A graph was then constructed, whereby nodes represented each neighbourhood partition combination, and edges are the distance (in the expression profile) between these partition combinations. This graph was then clustered with the Leiden graph clustering algorithm to identify integrated neighbourhoods. Hyperparameters for the above clustering process are provided in Supplementary Table 4. 3D neighbourhoods were displayed using the open-source visualization tool Napari (https://github.com/napari/napari).

Analysis and quantification of 3D neighbourhoods. Neighbourhoods were then assigned to Visium ST spots in the following manner. Each spot was assigned the neighbourhood label of the neighbourhood overlapping its spot centroid.

To focus on neighbourhoods most related to the TME biology, we filtered out neighbourhoods with >50% overlap with copy number annotated subclones. Additionally, we excluded neighbourhoods that mapped to fewer than ten total spots across all ST sections for a sample.

The subclone boundary region for tumour clones was defined as the union of the outermost layer of subclone annotated spots and the spots one layer expanded out from them, representing an area roughly 100–150 μm at the tumour–TME interface. Subclone-specific fractions were calculated as the neighbourhood overlaps with the outermost layer of each subclone.

In HT397B1, DEGs were calculated for all neighbourhoods, not only those filtered for subclone overlap and spot count. The top 50 DEGs for neighbourhoods 4 and 6 were grouped into three categories: shared, unique to neighbourhood 4 and unique to neighbourhood 6. For the display in Fig. 5, the top 10 for each group were selected for display based on the following sorting criteria. The mean expression delta between neighbourhoods 4 and 6 was calculated for each gene by subtracting the mean expression in neighbourhood 6 from neighbourhood 4. Shared DEGs were ordered in ascending fashion based on the absolute expression delta of each gene. Genes unique to neighbourhood 4 and neighbourhood 6 were ordered by mean expression delta in descending and ascending fashion, respectively.

Cell-type annotation of CODEX imaging data. Our workflow for cell annotation consisted of four main steps: (1) image format conversion, (2) cell segmentation, (3) spatial feature generation and (4) cell-type classification. First, we converted image output by the CODEX platform (.qptiff) to the popular open-source OME-TIFF format. During this process, we also produced a separate image for each sample, as multiple sections of tissue are sometimes included on the same imaging run. We then used the Mesmer pre-trained nuclei + membrane segmentation model in the DeepCell framework[75] to segment nuclei and whole cells. DAPI was used as the nuclei intensity image, and the channels pan-cytokeratin, HLA-DR, SMA, CD4, CD45, Hep-Par-1, CD31, E-cadherin, CD68 and CD3e were, for those present in a given image, mean-averaged to a single channel and used as the membrane intensity image.

We then use a gating procedure to identify cell types. First, to combat differences in protein intensity distributions between imaging runs and tissue types, thresholds were manually set for all protein channels used during cell typing for each image by visual inspection. Above this intensity threshold, a pixel was considered positive for a given marker, and below it, a pixel was considered negative. We then used the cell segmentation boundaries from the previous step to calculate the fraction of positive pixels for all cell typing markers in each cell. The result of this process is a feature matrix (num cells × num proteins) representing positive marker fractions for each cell typing protein in every cell. A cell was considered positive for a marker if >5% of its pixels were positive for that marker. Cells were then labelled with a gating strategy specific to each sample. During gating, each cell was subjected to a series of AND gates, whereby if a cell passed all criteria for a given step, it was annotated as the cell type specified for that step, whereas if it failed the criteria it was passed on to the next downstream step in the gating strategy. The gating strategies used for the samples in this paper are presented in Supplementary Table 4.

The following labels were the set of all possible cell type annotations: epithelial, CD4 T cell, CD8 T cell, regulatory T cell, T cell, macrophage, macrophage-M2, B cell, dendritic, immune, endothelial, fibroblast and hepatocyte. For some images, not all proteins required to gate a specific cell type were present. For example, CD4 was not in every image panel and available to use in the annotation of CD4 T cells. In these instances, the gating strategy was constructed such that cells can be labelled as more general cell types if specific proteins are not present (that is, labelled more broadly as T cell instead of CD4 T cell). If a cell was negative for all steps in the gating strategy, it was annotated as 'unlabelled'. The code for image format conversion and cell segmentation can be found at GitHub (https://github.com/estorrs/multiplex-imaging-pipeline).

Distance to tumour boundary quantification on CODEX. After registration, Visium spots labelled as tumours were mapped to CODEX slides using the coordinates of the aligned images. The coordinates of the centre of each spot in the CODEX-aligned slide were the same as its Visium counterpart. Each spot in the CODEX-aligned slide occupied the area of a circle with a radius of 150 pixels. The Euclidean distance transforms in the CODEX-aligned slide were then calculated for each pixel using Python's scipy.ndimage.distance_transform_edt. Both the distances from the microregions and within the microregions were calculated.

3D tumour volume reconstruction and location quantification. The surface mesh visualizations of the tumour volumes for HT397B1 and HT268B1 were generated using the following steps: (1) tumour neighbourhood selection, (2) mesh construction and (3) mesh colouring. First, integrated neighbourhoods with tumour metrics (described below) exceeding a given threshold were considered to be part of the tumour volume. In HT268B1, the metric used to quantify epithelial character was the fraction of subclone annotated Visium ST spots per neighbourhood. Neighbourhoods with >60% subclone spots were considered tumour. In HT397B1, we instead used the fraction of CODEX-annotated epithelial cells, as CODEX sections outnumbered the Visium ST sections for that sample. Neighbourhoods with >60% fraction of epithelial cells were considered tumour.

A new volume was then constructed whereby neighbourhoods classified as tumour neighbourhoods using the above criteria were considered tumour-positive voxels, and all other voxels were tumour-negative. This 3D tumour mask was then smoothed with a Gaussian kernel (sigma = 1.0). The resulting values were then used as input for the marching cubes algorithm[76,77] to generate a surface mesh for the tumour volume. We used the scikit-image implementation (skimage.measure.marching_cubes) of the marching cubes algorithm with default parameters.

To colour the surface mesh, we generated 3D feature volumes (described below), and then coloured points on the surface mesh based on the voxel value at the corresponding location in the feature volume. A feature volume is a volume whereby each voxel in the volume describes some feature from the serial section dataset (for example, expression of a given gene, fraction of cells, and so on). Feature volumes used in this analysis were constructed in the following manner. First, in the serial sections for which a feature was applicable, the feature was binned at the same resolution as the 3D neighbourhoods (50 μm in this case). The binned feature was then interpolated in the *z* direction to fill in gaps between sections. The resulting volume was of the same shape as the integrated neighbourhood volume, for which the value of each voxel was the aggregated feature count for the voxel. For HT268B1, the features used were logged expression of *TYMP1* and *IGLC2*. For HT397B1, we used fibroblast and immune cell fraction. Cells were annotated as described in the section 'Cell-type annotation of CODEX imaging data'. The surface mesh was visualized using Napari (https://github.com/napari/napari) and contrast was adjusted on a volume-to-volume basis. We also visualized the HT397B1 tissue volume with the Imaris platform, for which we generated surfaces from the following CODEX markers: pan-cytokeratin (epithelial), CD45 (immune) and SMA (stromal).

Xenium probe design. Custom Xenium gene and mutation probes were designed using Xenium Panel Designer (https://cloud.10xgenomics.com/xenium-panel-designer) following instructions outlined in the 'Getting Started with Xenium Panel Design' instructions (https://www.10xgenomics.com/support/in-situ-gene-expression/documentation/steps/panel-design/xenium-panel-getting-started#design-tool). In brief, 21-bp sequences flanking the targeted transcribed variant site were curated from the Ensembl canonical transcript (Ensembl v.100). All four possible ligation junctions (two for the WT allele and two for the variant allele, three in the case of deletions—two for the WT allele and one for the variant allele) were then evaluated. Variant sites for which only non-preferred junctions (CG, GT, GG and GC) were available were excluded. The two bases of the ligation junction sequence were the last base of the RBD5 (RNA binding domain) and the first base of the RBD3 probe. Preferred junctions were always prioritized over neutral junctions unless a neutral junction was necessary to avoid hairpins, homopolymer regions, dimers or an unfavourable annealing temperature. Probe lengths for RBD5 and RBD3 were then adjusted from the 21-bp starting length to target a temperature between 50 °C and 70 °C per probe (overall target 68 °C and 82 °C). Variant sites with probes predicted to form dimers or hairpins by IDT's oligo analyzer were excluded. Variant sites with homopolymer regions of five consecutive bases or more in either the RBD5 or RBD3 probes were excluded.

Spatial expression deconvolution. Here we used both deconvolution results and cell-type-specific expressions in the snRNA-seq data to deconvolve the Visium ST expression data (Supplementary Fig. 9). In brief, for a given Gene1, we first calculated the average expression of Gene1 per cell type in matched snRNA-seq data, subsequently filtering out the expression of such genes in cell types having <5% of the highest average expression, and then dividing each cell-type average expression from the sum of all average expressions, thereby creating the expression contribution per cell type matrix (Q). Then for a given spot, the contribution per cell type was multiplied by cell type proportion from the cell type devolution result (for example, RCTD), then normalized to 1 to give a final expression contribution matrix (WN). For instance, in Supplementary Fig. 9a, Gene1 has 40%, 30% and 30% contributions from respective cell types A, B and C based on the filtered snRNA-seq expression. For Spot1, as there is only 1 cell type, B, in the spot, 40% × 1/40% × 1 gives the final 100% contribution of Gene1 to cell type B in Spot1. Spot2 contains 50% A and B cell types, respectively, the normalized cell type contribution in spot 2 is therefore 50% × 40%/(50% × 40% + 50% × 30%) ≈ 57.1% for the cell type A, and 50% × 30%/(50% × 40% + 50% × 30%) ≈ 42.9% for the cell type B. The final deconvolved expression was obtained by multiplying the original expression per spot (5 and 20 in Spot1 and Spot2) with the respective cell-type-based contribution to obtain the final deconvoluted expression values of Spot1 – cell type B = 5, Spot2 – cell type A ≈ 10.42, and Spot2 – cell type B ≈ 8.58.

Reporting summary

Further information on research design is available in the Nature Portfolio Reporting Summary linked to this article.

Data availability

Visium, scRNA-seq, snRNA-seq, WES, Xenium and CODEX imaging data are part of HTAN dbGaP study accession phs002371.v3.p1 (https://www.ncbi.nlm.nih.gov/projects/gap/cgi-bin/study.cgi?study_id=phs002371.v3.p1), and the data can be accessed through the HTAN DCC Portal (https://data.humantumoratlas.org/) under the HTAN WUSTL Atlas. Individual samples can be identified using Biospecimen ID from the Sample_ID_Lookup_table.xlsx on the GitHub page (https://github.com/ding-lab/ST_subclone_publication). GRCh38 references used for scRNA-seq and snRNA-seq (refdata-gex-GRCh38-2020-A) are freely available from the 10x Genomics website (https://support.10xgenomics.com). The reference GRCh38 genome (GRCh38.d1.vd1.fa.tar.gz) used for WES reads alignment is available from GDC (https://gdc.cancer.gov/about-data/gdc-data-processing/gdc-reference-files). The MSigDB hallmark gene sets is available from the GSEA website (https://www.gsea-msigdb.org/gsea/msigdb/collections.jsp). The L1000 perturbation database is available through the resource page on the Harmonizome website (https://maayanlab.cloud/Harmonizome/resource/LINCS+L1000+Connectivity+Map) and the library page on the Enrichr website https://maayanlab.cloud/Enrichr/#libraries).

Code availability

All bioinformatics programs used in this study can be accessed from the GitHub public repository (https://github.com/ding-lab/ST_subclone_publication). The code for 3D neighbourhood identification and construction is available at GitHub (https://github.com/ding-lab/mushroom/tree/subclone-resubmission). The code for multiplex imaging processing is hosted at GitHub (https://github.com/estorrs/multiplex-imaging-pipeline). The code for Morph is accessible at GitHub (https://github.com/ding-lab/morph).

46. Herndon, J., Fields, R., Zhou, D. C. & Ding, L. Biospecimen collection and processing 2.0. *protocols.io* https://doi.org/10.17504/protocols.io.bszynf7w (2021).
47. Wu, Y. et al. Epigenetic and transcriptomic characterization reveals progression markers and essential pathways in clear cell renal cell carcinoma. *Nat. Commun.* **14**, 1681 (2023).
48. Houston, A., Chen, S. & Chen, F. Spatial transcriptomics for OCT using 10x Genomics Visium. *protocols.io* https://doi.org/10.17504/protocols.io.x54v9d3opg3e/v1 (2023).
49. Houston, A., Chen, S. & Chen, F. Spatial transcriptomics for FFPE utilizing 10x Genomics Visium. *protocols.io* https://doi.org/10.17504/protocols.io.kxygx95ezg8j/v1 (2023).
50. Caravan, W., Jayasinghe, R. & Al Deen, N. N. WU sn-prep protocol for solid tumors—snRNA protocol v2.8. *protocols.io* https://doi.org/10.17504/protocols.io.14egn7w6zv5d/v1 (2022).
51. Jayasinghe, R., Caravan, W., Houston, A. & AlDeen, N. N. WU sn-prep protocol for solid tumors—joint snRNA+ATAC v2.9. *protocols.io* https://doi.org/10.17504/protocols.io.261gednx7v47/v1 (2023).
52. Jayasinghe, R., Ding, L. & Chen, F. WU sc-prep protocol for solid tumors v2.1. *protocols.io* https://doi.org/10.17504/protocols.io.bsnqnddw (2021).
53. Jayasinghe, R., Ding, L., Chen, F. & Satok. Bulk DNA extraction (Ding Lab). *protocols.io* https://doi.org/10.17504/protocols.io.bsnhndb6 (2021).
54. Kim, S. et al. Strelka2: fast and accurate calling of germline and somatic variants. *Nat. Methods* **15**, 591–594 (2018).
55. Cibulskis, K. et al. Sensitive detection of somatic point mutations in impure and heterogeneous cancer samples. *Nat. Biotechnol.* **31**, 213–219 (2013).
56. Koboldt, D. C. et al. VarScan 2: somatic mutation and copy number alteration discovery in cancer by exome sequencing. *Genome Res.* **22**, 568–576 (2012).
57. Ye, K., Schulz, M. H., Long, Q., Apweiler, R. & Ning, Z. Pindel: a pattern growth approach to detect break points of large deletions and medium sized insertions from paired-end short reads. *Bioinformatics* **25**, 2865–2871 (2009).
58. Bailey, M. H. et al. Comprehensive characterization of cancer driver genes and mutations. *Cell* **173**, 371–385.e18 (2018).
59. Li, Y. et al. Pan-cancer proteogenomics connects oncogenic drivers to functional states. *Cell* **186**, 3921–3944.e25 (2023).
60. Terekhanova, N. V. et al. Epigenetic regulation during cancer transitions across 11 tumour types. *Nature* **623**, 432–441 (2023).
61. McKenna, A. et al. The Genome Analysis Toolkit: a MapReduce framework for analyzing next-generation DNA sequencing data. *Genome Res.* **20**, 1297–1303 (2010).
62. Quinlan, A. R. & Hall, I. M. BEDTools: a flexible suite of utilities for comparing genomic features. *Bioinformatics* **26**, 841–842 (2010).
63. Ma, C. et al. Inferring allele-specific copy number aberrations and tumor phylogeography from spatially resolved transcriptomics. Preprint at *bioRxiv* https://doi.org/10.1101/2024.03.09.584244 (2024).
64. Liberzon, A. et al. The Molecular Signatures Database (MSigDB) hallmark gene set collection. *Cell Syst.* **1**, 417–425 (2015).
65. Subramanian, A. et al. A next generation connectivity map: L1000 platform and the first 1,000,000 profiles. *Cell* **171**, 1437–1452.e17 (2017).
66. Kuleshov, M. V. et al. Enrichr: a comprehensive gene set enrichment analysis web server 2016 update. *Nucleic Acids Res.* **44**, W90–W97 (2016).
67. Liu, B. et al. An entropy-based metric for assessing the purity of single cell populations. *Nat. Commun.* **11**, 3155 (2020).
68. Hao, Y. et al. Integrated analysis of multimodal single-cell data. *Cell* **184**, 3573–3587.e29 (2021).
69. Cang, Z. et al. Screening cell–cell communication in spatial transcriptomics via collective optimal transport. *Nat. Methods* **20**, 218–228 (2023).
70. Liu, X., Zeira, R. & Raphael, B. J. Partial alignment of multislice spatially resolved transcriptomics data. *Genome Res.* **33**, 1124–1132 (2023).
71. Bogovic J. A., Hanslovsky P., Wong A., Saalfeld S. in *2016 IEEE 13th International Symposium on Biomedical Imaging (ISBI)*, 1123–1126 (2016)
72. Dosovitskiy, A. et al. An image is worth 16x16 words: transformers for image recognition at scale. Preprint at https://doi.org/10.48550/arXiv.2010.11929 (2021).
73. He, K. et al. in *2022 IEEE/CVF Conference on Computer Vision and Pattern Recognition (CVPR)* 15979–15988 (IEEE, 2022).
74. Pérez-García, F., Sparks, R. & Ourselin, S. TorchIO: a Python library for efficient loading, preprocessing, augmentation and patch-based sampling of medical images in deep learning. *Comput. Methods Programs Biomed.* **208**, 106236 (2021).
75. Greenwald, N. F. et al. Whole-cell segmentation of tissue images with human-level performance using large-scale data annotation and deep learning. *Nat. Biotechnol.* **40**, 555–565 (2022).
76. Lewiner, T., Lopes, H., Vieira, A. W. & Tavares, G. Efficient implementation of marching cubes' cases with topological guarantees. *J. Graph. Tools* https://doi.org/10.1080/10867651.2003.10487582 (2012).
77. Lorensen, W. E. & Cline, H. E. Marching cubes: a high resolution 3D surface construction algorithm. *ACM SIGGRAPH Comp. Graph.* **21**, 163–169 (1987).

Acknowledgements This work was performed as part of the NCI Human Tumor Atlas Network (HTAN). We thank the patients, staff and scientists who contributed to this study; staff at HTAN member centres, the Clinical Proteomics Tumor Analysis Consortium and the Siteman Cancer Center at Washington University for their support; and I. Strunilin, J. Wang, Y. Li, W.-W. Liang and Y. Li for their feedback on the manuscript. The following grants supported this work: U2CCA233303 to L.D., R.C.F. and W.E.G.; U54AG075934 to L.D., R.C.F. and F.C.; U24CA210972 to L.D.; R01NS107833 and R01NS117149 to M.G.C.; R01HG009711 and R01CA260112 to L.D. and F.C.; U24CA209837 to K.I.S.; K12CA167540 to L.-I.K; and NIH/NCI grants U24CA248453 and U24CA264027 to B.J.R. C.M. is a Damon Runyon Fellow supported by the Damon Runyon Cancer Research Foundation (DRQ-15-22).

Author contributions Study conception and design: L.D., F.C., B.J.R., R.C.F. and W.E.G. Developed and performed experiments or data collection: S.C., A.S., A. Houston, J.M., R.G.J., S.P.G., A.T.M.A.A., P.B., J.M. Herndon, W.E.G., R.C.F., R.P., F.C. and L.D. Computation and statistical analyses: C.-K.M., J.L., E.S., A.L.N.T.d.C., C.M., X.L. and M.C.W. Data interpretation a biological analyses: C.-K.M., J.L., S.C., E.S., A.L.N.T.d.C., A.K., A.N.S.-S., L.F., S.L., M.B., A. Hill, J.E.I., V.T., J.M. Held, I.S.H., E.H.K., P.O.B., A.H.K., M.M.M., K.I.S., S.V.P., T.J., M.A.R., C.W., L.-I.K., D.J.V., M.G.C., R.P., K.C.F., W.E.G., R.C.F., R.G.J., B.J.R., F.C. and L.D. Writing: C.-K.M., J.L., S.C., E.S., A.L.N.T.d.C., M.D.I., L.D. and M.C.W. Administration: F.C. and L.D.

Competing interests The authors declare no competing interests.

Additional information

Supplementary information The online version contains supplementary material available at https://doi.org/10.1038/s41586-024-08087-4.

Correspondence and requests for materials should be addressed to William E. Gillanders, Ryan C. Fields, Benjamin J. Raphael, Feng Chen or Li Ding.

Peer review information *Nature* thanks Moritz Gerstung, Artem Lomakin, Christian Schürch and the other, anonymous, reviewer(s) for their contribution to the peer review of this work.

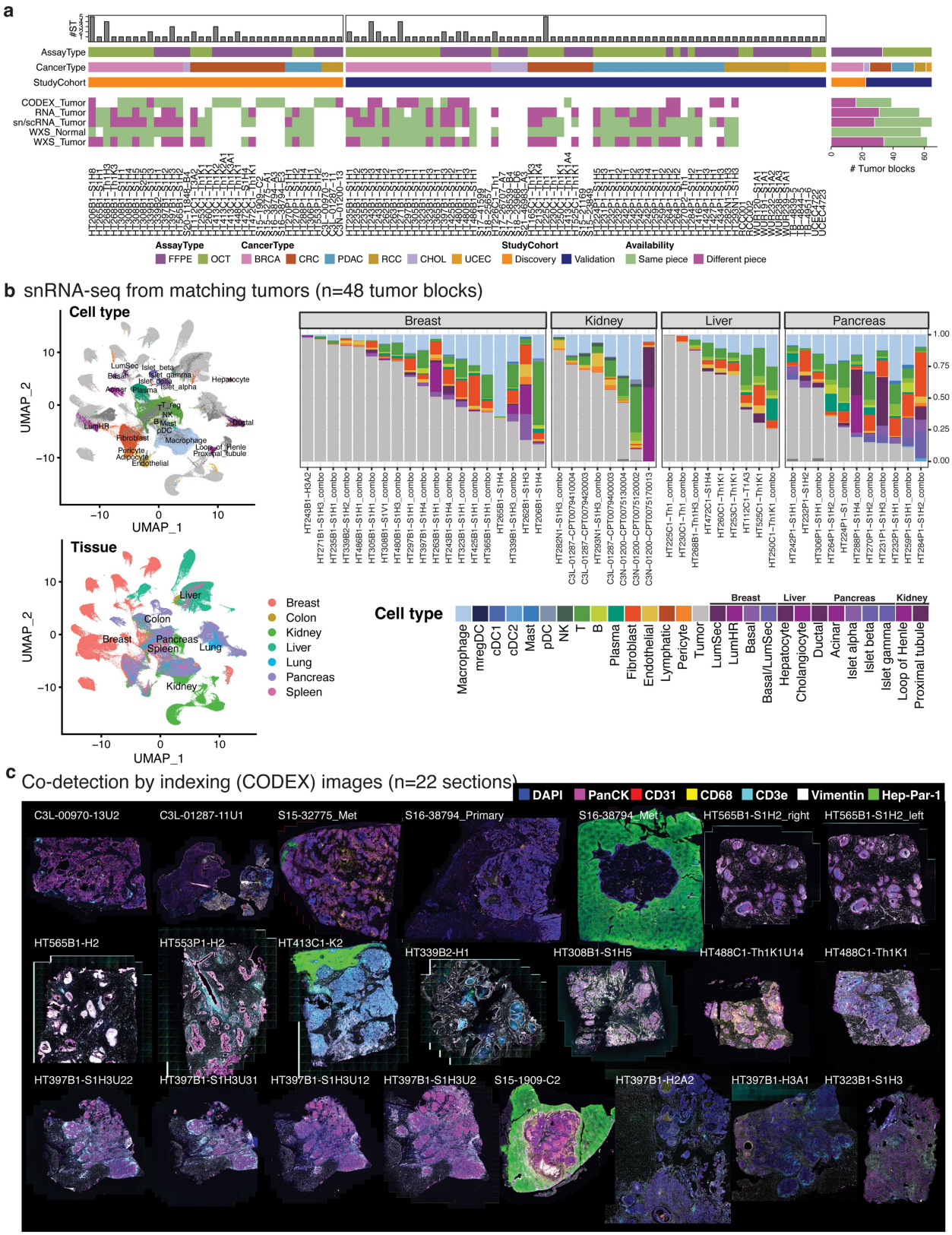

Extended Data Fig. 1 | Data Overview in Spatial Tumor Cohorts. a, Overview of the data availability of the spatial tumor cohort with assay types, cancer types, and study cohort. **b**, 48 snRNA-seq from matching tumor blocks across 7 tissue types (left). Cell type distribution from multi-sample tissue types (right). **c**, 22 Co-detection by indexing (CODEX) multiplexed immunofluorescence imaging from matching tumor sections.

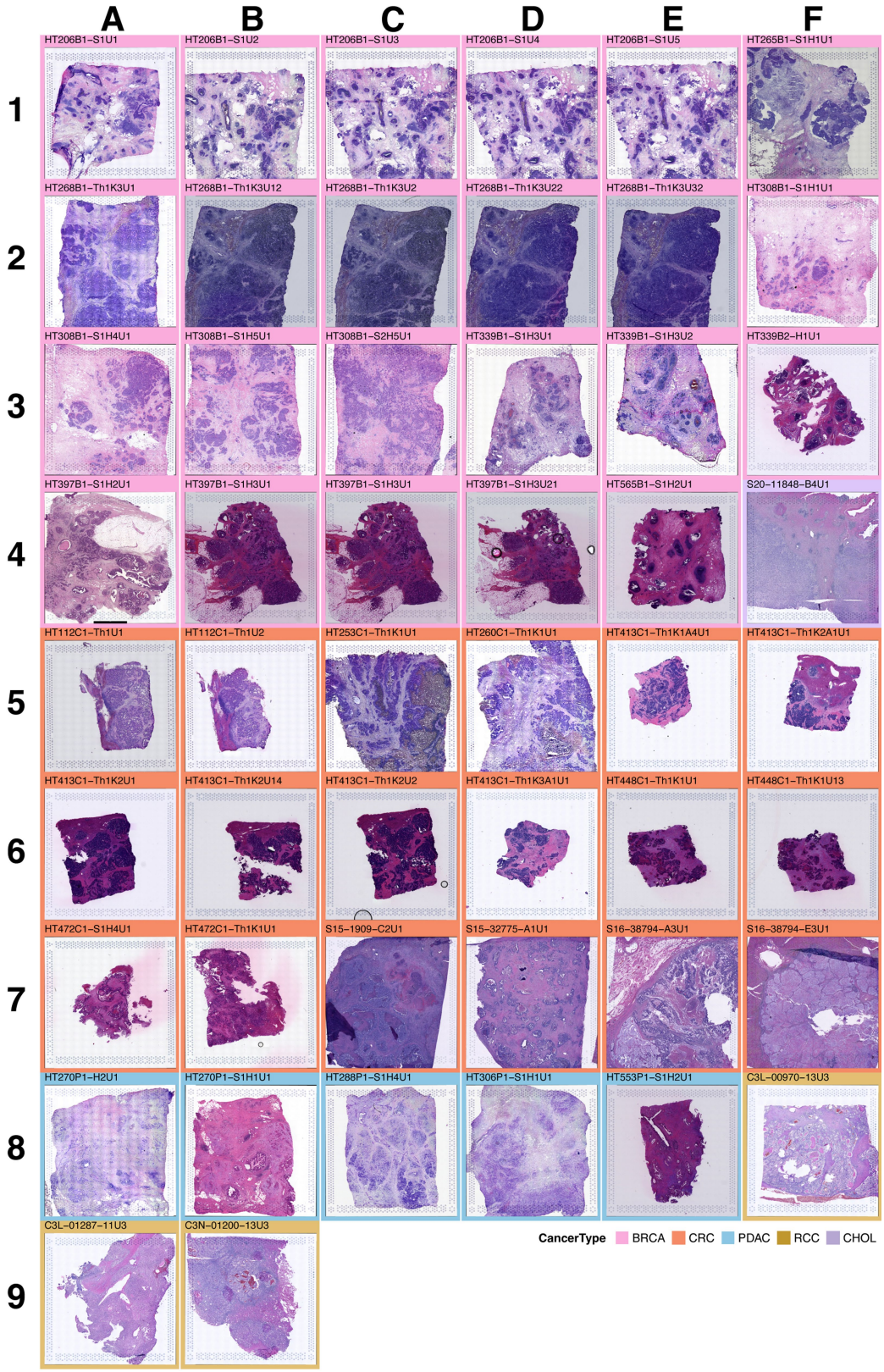

Extended Data Fig. 2 | Histology of the Spatially Distinct Cohort. Histology of the spatially distinct cohort colored by cancer type. Light pink BRCA (n = 23), light purple CHOL (n = 1), orange CRC (n slice = 18), light blue PDAC (n = 5), and light brown RCC (n = 3).

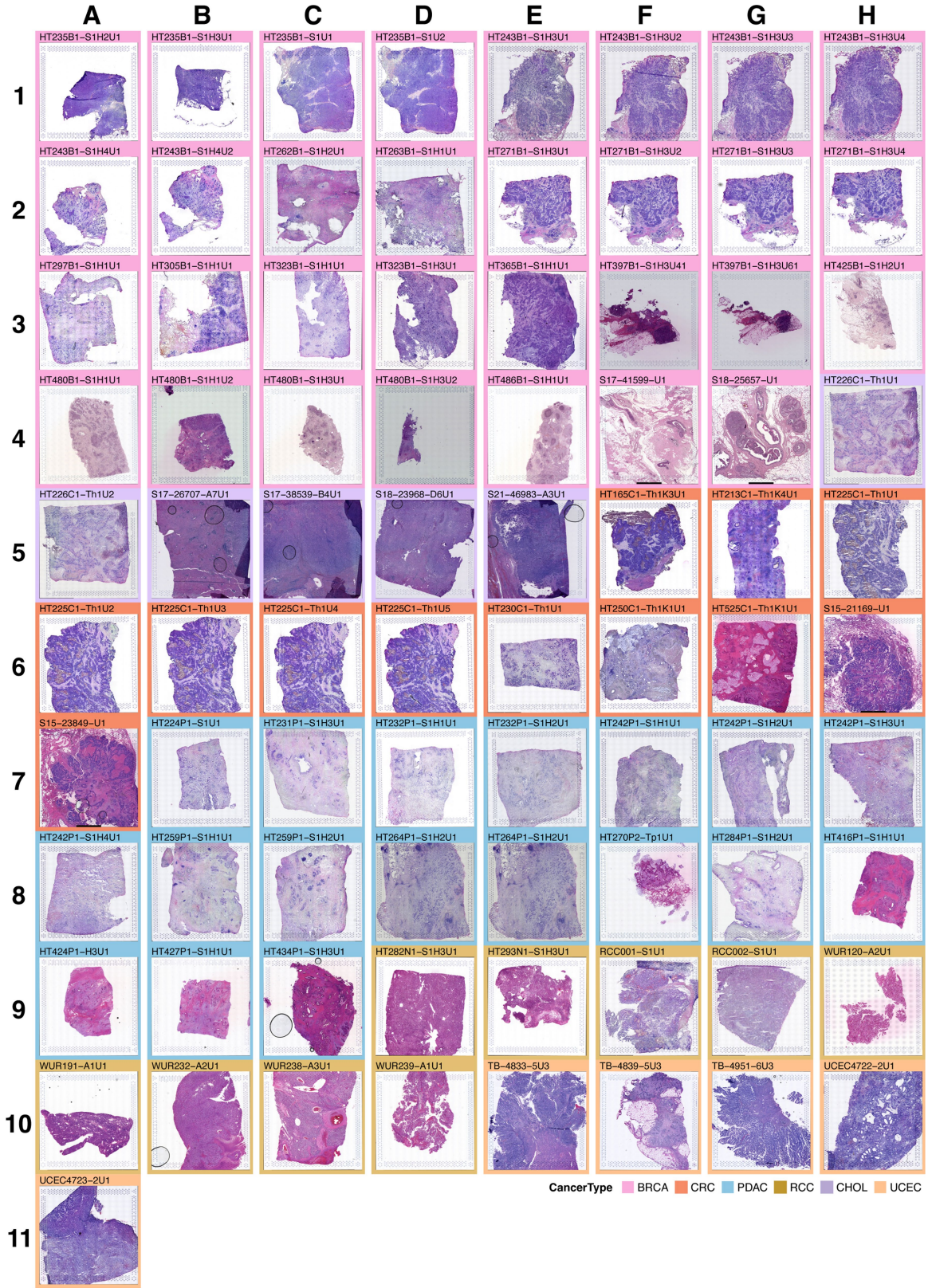

Extended Data Fig. 3 | Histology of the Spatially Diffuse Cohort. Histology of the spatially diffuse cohort colored by cancer types. Light pink BRCA (n = 31), light purple CHOL (n = 6), orange CRC (n = 12), light blue PDAC (n = 18), light brown RCC (n = 9), and pale orange UCEC (n = 5).

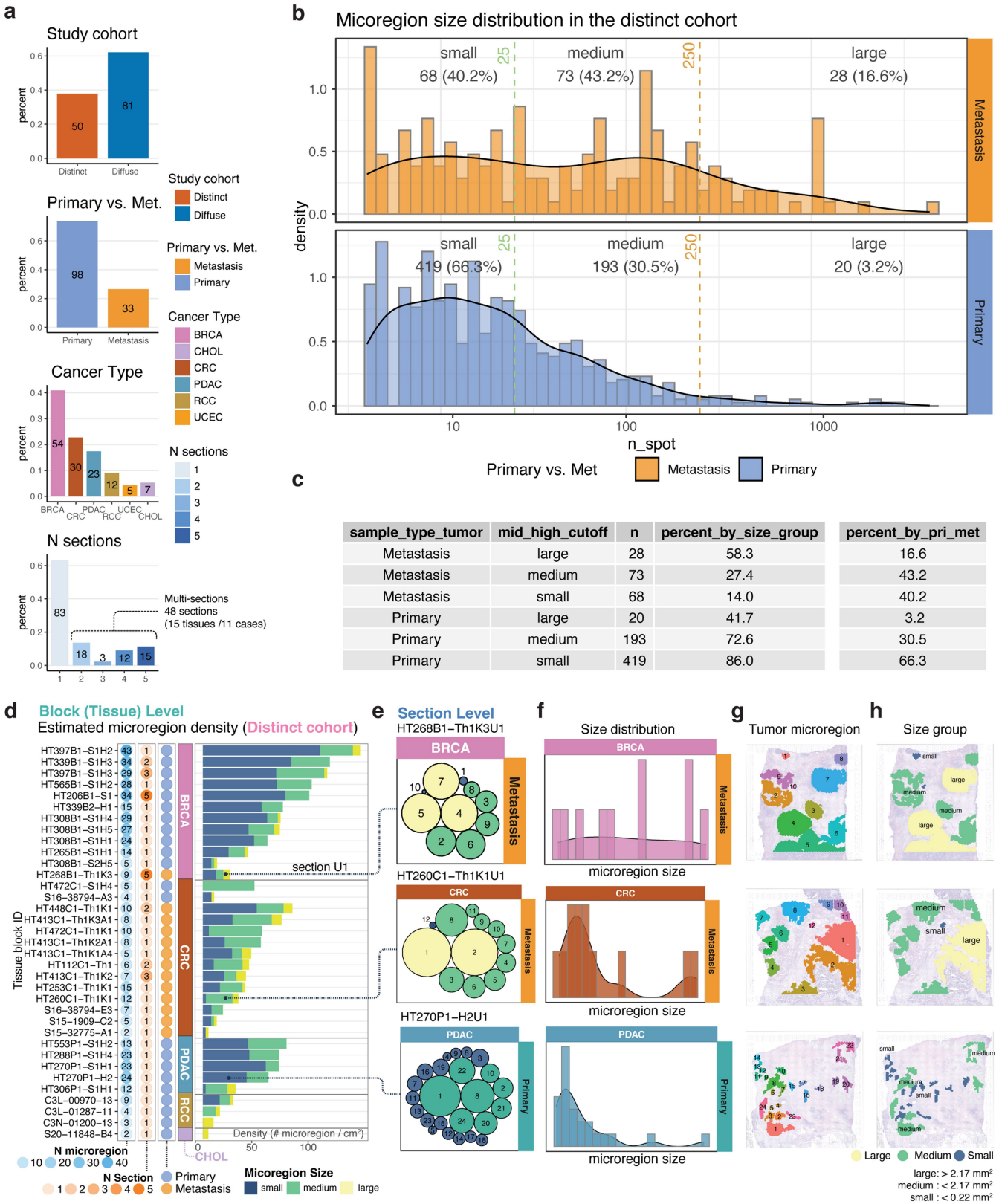

sample_type_tumor	mid_high_cutoff	n	percent_by_size_group	percent_by_pri_met
Metastasis	large	28	58.3	16.6
Metastasis	medium	73	27.4	43.2
Metastasis	small	68	14.0	40.2
Primary	large	20	41.7	3.2
Primary	medium	193	72.6	30.5
Primary	small	419	86.0	66.3

Extended Data Fig. 4 | Microregion Distribution and Characteristics across Cohorts. a, Sample count distribution for each cohort, primary vs. metastasis, cancer type, and count of section per sample. **b**, microregion size distribution between primary and metastasis samples (primary n = 98 sections from 60 cases; metastasis n = 33 sections from 16 cases). **c**, table with the count of microregions per size. **d**, Estimated microregion density per tissue block. The number of microregions, sections, and primary vs metastasis status, cancer of each block is indicated on the left. **e**, Example microregion sizes, **f**, size distribution histograms, and **g**, microregion and **h**, size groups visualized on Visium ST for HT268B1-Th1K3U1 (BRCA), HT260C1-Th1K1U1 (CRC), and HT270P1-H2U1 (PDAC).

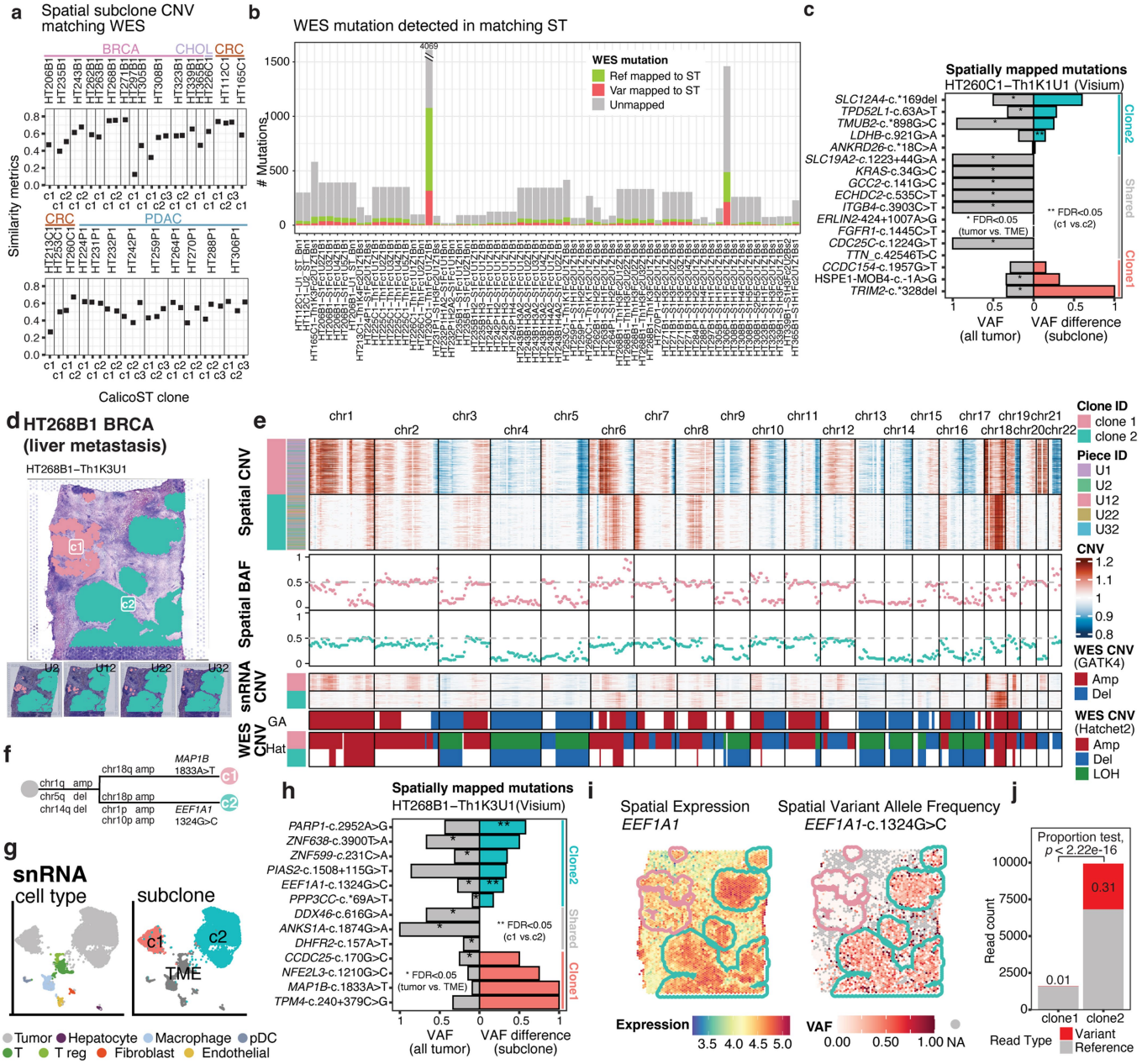

Extended Data Fig. 5 | Genomic Profiling of Spatial Subclones. a, Spatial subclone genome-wide CNV profile similarity compared with matching WES-inferred CNV. **b**, Distribution of variants mapped to ST transcripts out of all somatic mutations detected from matching WES. Ref: reference allele; Var: variant allele. **c**, Somatic mutations mapped to HT260C1 are shared and unique to two spatial subclones. For each WES-derived mutation, VAFs between tumor and non-tumor regions (binomial test, left) and VAFs between two spatial subclones (proportion test, right) were compared. Mutations with FDR<0.05 (Benjamini & Hochberg correction) were annotated with * and ** for VAF and VAF differences, respectively. **d**, A breast cancer liver metastasis sample (HT268B1) showing 2 spatial subclones across 5 sections. **e**, In the heatmap (top), estimated somatic copy number variations (CNV) per spot show both shared and unique CNV events between the two spatial subclones. The b-allele frequencies (BAF) in each spatial subclone from the same genomic window are shown in the middle tracks, while the snRNA- and WES-inferred CNV status of the same genomic window is shown in the bottom tracks. **f**, The predicted phylogenetic relationship of the 2 tumor spatial subclones. **g**, UMAP of matching snRNA showing cell types and two tumor subclones. **h**, Somatic mutations mapped to HT268B1 are shared and unique to two spatial subclones. VAF calculations and their statistical analyses are the same as in panel c. **i-j**, Subclonal mutation *EEF1A1*.1324G>C is uniquely detected in Clone2 in spatial transcriptomics, while *EEF1A1* expression is in both spatial subclones ($p < 2.22 \times 10^{-16}$, two-sided proportion test).

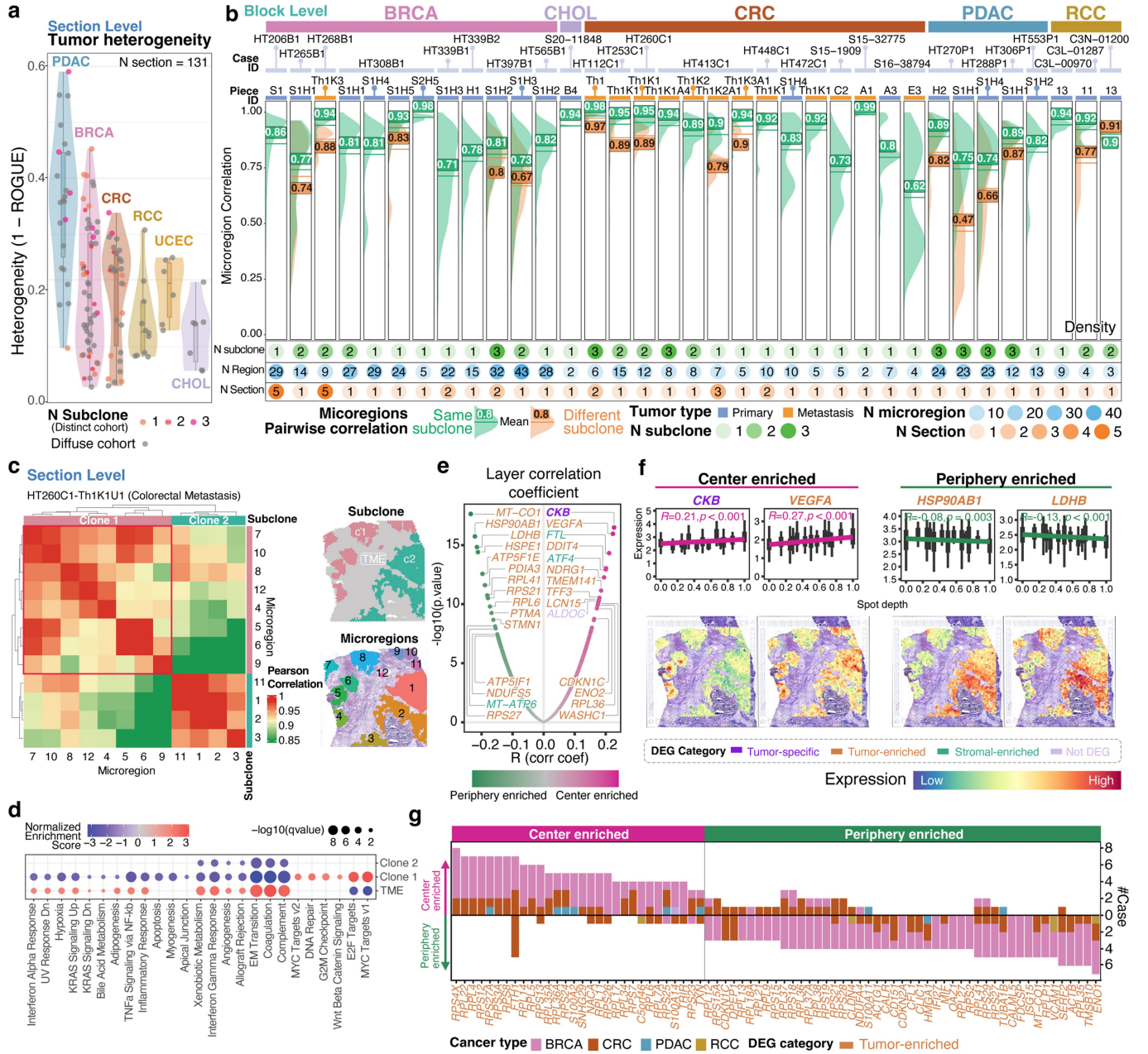

Extended Data Fig. 6 | Spatial Expression Pattern of Tumor Microregions Driven by Genetic Alteration and Tumor Depth. a, Tumor heterogeneity evaluated by 1- ROGUE scoring. Higher scores indicate higher heterogeneities. Each point represents one section and is colored by its respective cohort designation and number of subclones (n = 131 sections from 78 cases). The box plot's center line represents the median, with the lower and upper hinges indicating the first and third quartiles. Whiskers extend to the highest and lowest values within 1.5 times the interquartile range (IQR) from the hinges. **b**, (Top panel) Distribution of pairwise Pearson correlations between pairs of microregions within the same section. Distribution is split by those from the same tumor subclone (green) and those from different subclones (orange). The number in the boxes and the solid line indicate the mean of each distribution. (Bottom panel) Number of tumor subclones, microregions, and sections per tissue block. **c**. Pairwise Pearson correlation of microregions based on the top 500 most variable genes in section U1 of HT260C1-Th1H3. The red box highlights the pairwise Pearson correlations of microregions within Clone 1. **d**, Pathway enrichment scores for Clone 1 (c1), and Clone 2 (c2), and TME, where bubble size represents corrected p-value (two-sided Wilcoxon rank-sum test FDR adjusted). **e**, Partial correlation coefficient rho (with tumor purity as a covariate) and $-\log_{10}$(p-value) between expression level and layer for all genes in the same section. Positive correlation indicates higher expression in the tumor center and negative correlation indicates higher expression in the tumor periphery. Genes are categorized using matching snRNA-seq as follows: purple for tumor-specific, orange for tumor-enriched, green for stromal-enriched, and light purple for not DEG. **f**, Center- and periphery-enriched genes with their correlation lines and spatial expression patterns (Pearson correlation). **g**, Top shared center- and periphery-enriched genes across cancer types (FDR<0.05 and rho>0.1 or rho<−0.1) (partial correlation with Benjamini-Hochberg procedure).

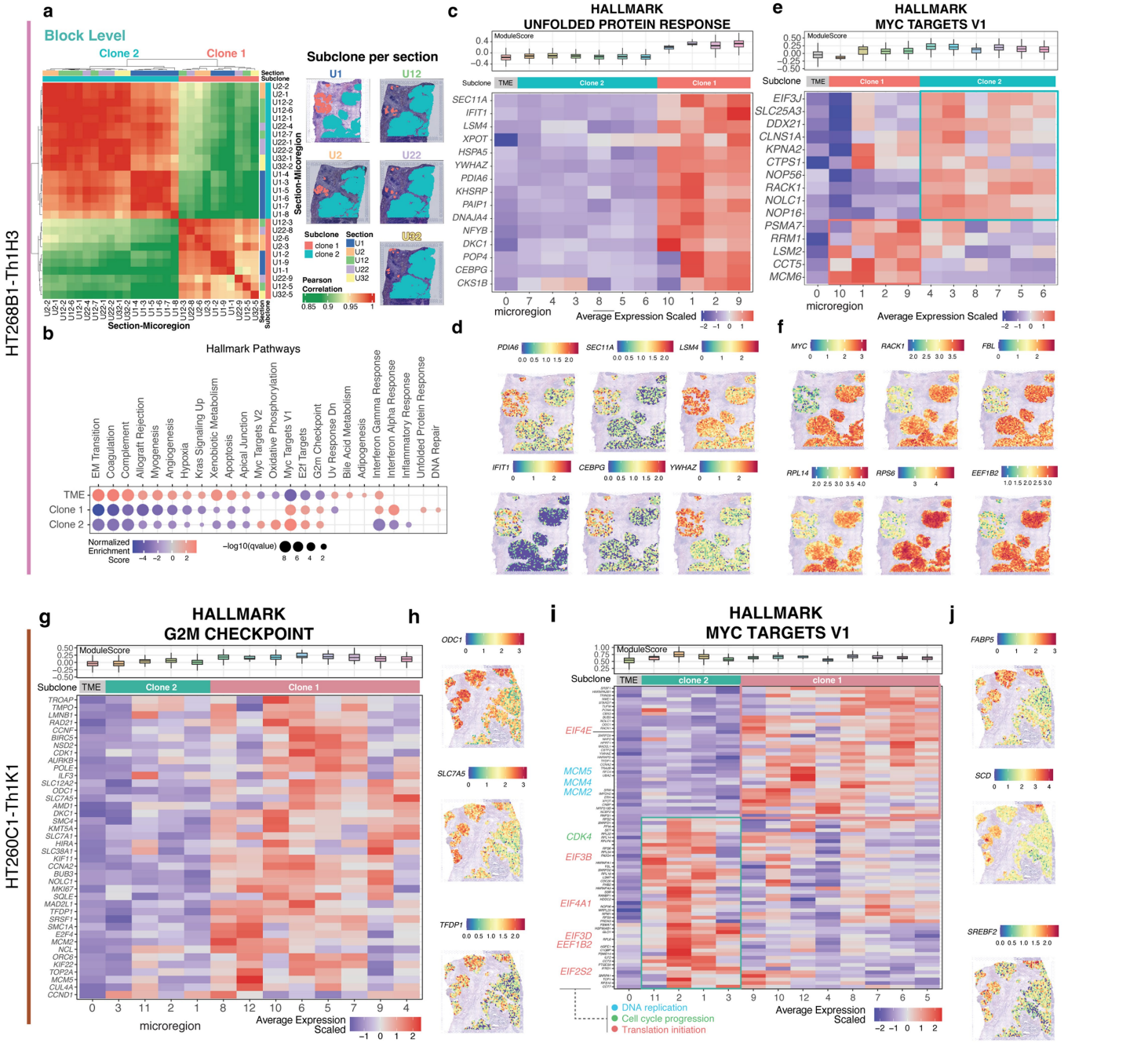

Extended Data Fig. 7 | Transcriptional Variability and Pathway Enrichment in Tumor Subclones. a, Pairwise Pearson correlation of the top 500 most variable genes in all 5 sections of Block HT268B1-Th1H3. Microregions with less than 10 spots were filtered out for this analysis. **b**, GSEA hallmark pathway enrichment analysis of tumor subclones compared to TME in the first section (U1) of HT268B1-Th1H3 (Two-sided Wilcoxon rank-sum test FDR adjusted). Average gene expression of upregulated genes in subclones from GSEA analysis and example spatial expression in **c**, **d**, Unfolded protein response, and **e**, **f**, MYC target v1 gene set in the first section (U1). **g**, **h**, G2M checkpoint, and **i**, **j**, MYC target v1 gene set. (i) Genes involved in DNA replication (light blue), cell cycle progression (light green), and translation initiation (light red) are highlighted. Average gene expression of upregulated genes in subclones from GSEA analysis and example spatial expression in **c, e, g, i**, (top panels) Module score, or average expression level of the program, calculated with Seurat AddModuleScore function (Method) using genes listed in each heatmap. The box plot's center line represents the median, with the lower and upper hinges indicating the first and third quartiles. Whiskers extend to the highest and lowest values within 1.5 times the interquartile range (IQR) from the hinges.

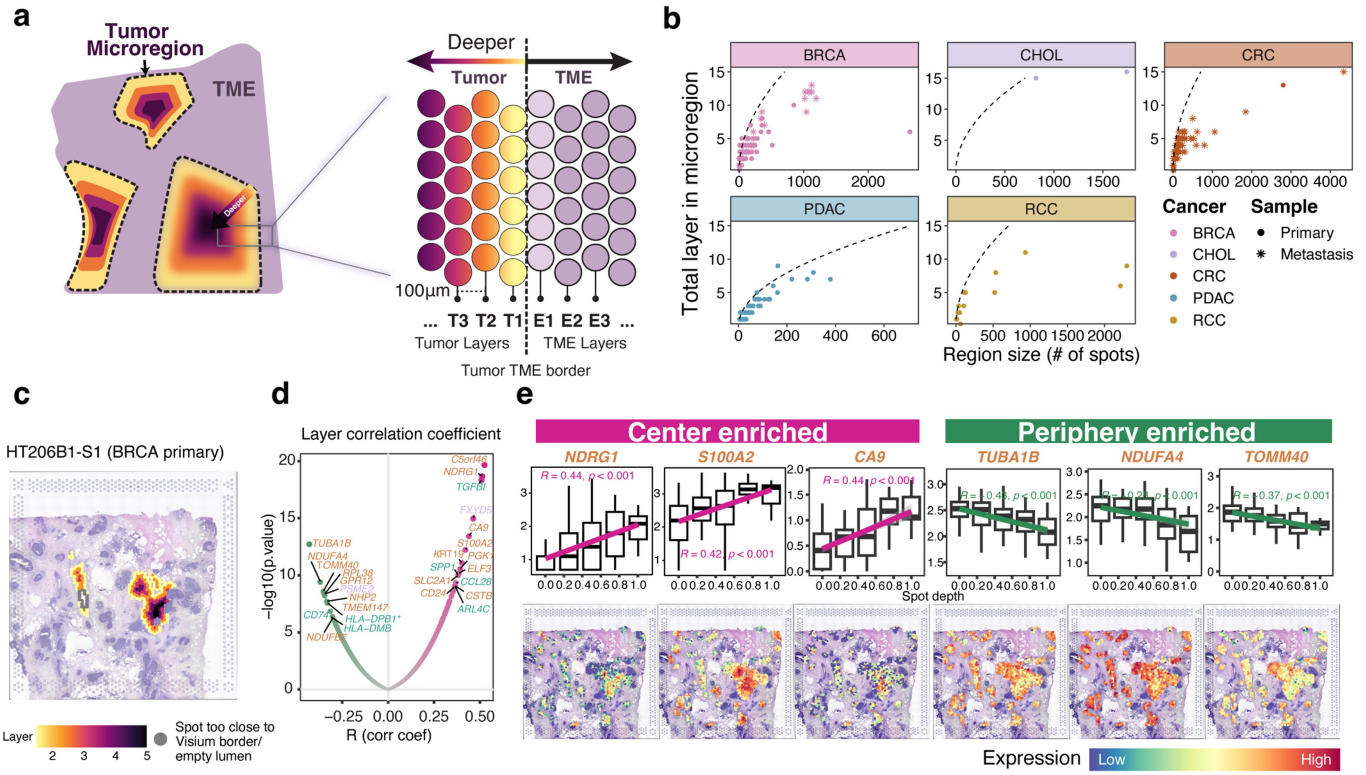

Extended Data Fig. 8 | Layer Depth and Gene Expression in Tumor Microregions. a, Schema of tumor depth designation for tumor microregions quantified in the number of layers. Starting from the tumor/TME border, proximal layers of tumor spots are iteratively defined as T1, T2, T3, etc, and distal TME spots are similarly defined as E1, E2, E3, etc. **b**, Relationship between the depth (measured in a total number of layers) and size (measured in the number of spots) of each microregion. The dashed reference line represents the projected depth-size relationship of perfect circular regions. **c**, A primary breast cancer sample with two tumor microregions eligible for the layer correlation analysis. Spots excluded from the analysis due to their proximity to the physical edge of the tissue are labeled in gray. **d**, Partial correlation coefficient rho (with tumor purity as covariate) and -$\log_{10}$(p-value) between expression levels and layers for all genes. Positive correlation indicates higher expression in the tumor center and negative correlation indicates higher expression in the tumor periphery. **e**, Top center- and periphery-enriched genes with their correlation lines and spatial expression patterns (Pearson correlation). The box plot's center line represents the median, with the lower and upper hinges indicating the first and third quartiles. Whiskers extend to the highest and lowest values within 1.5 times the interquartile range (IQR) from the hinges. Using Spatial Expression Deconvolution method to infer cell-type-specific expression yielded nearly identical results (Supplementary Fig. 9 and Methods).

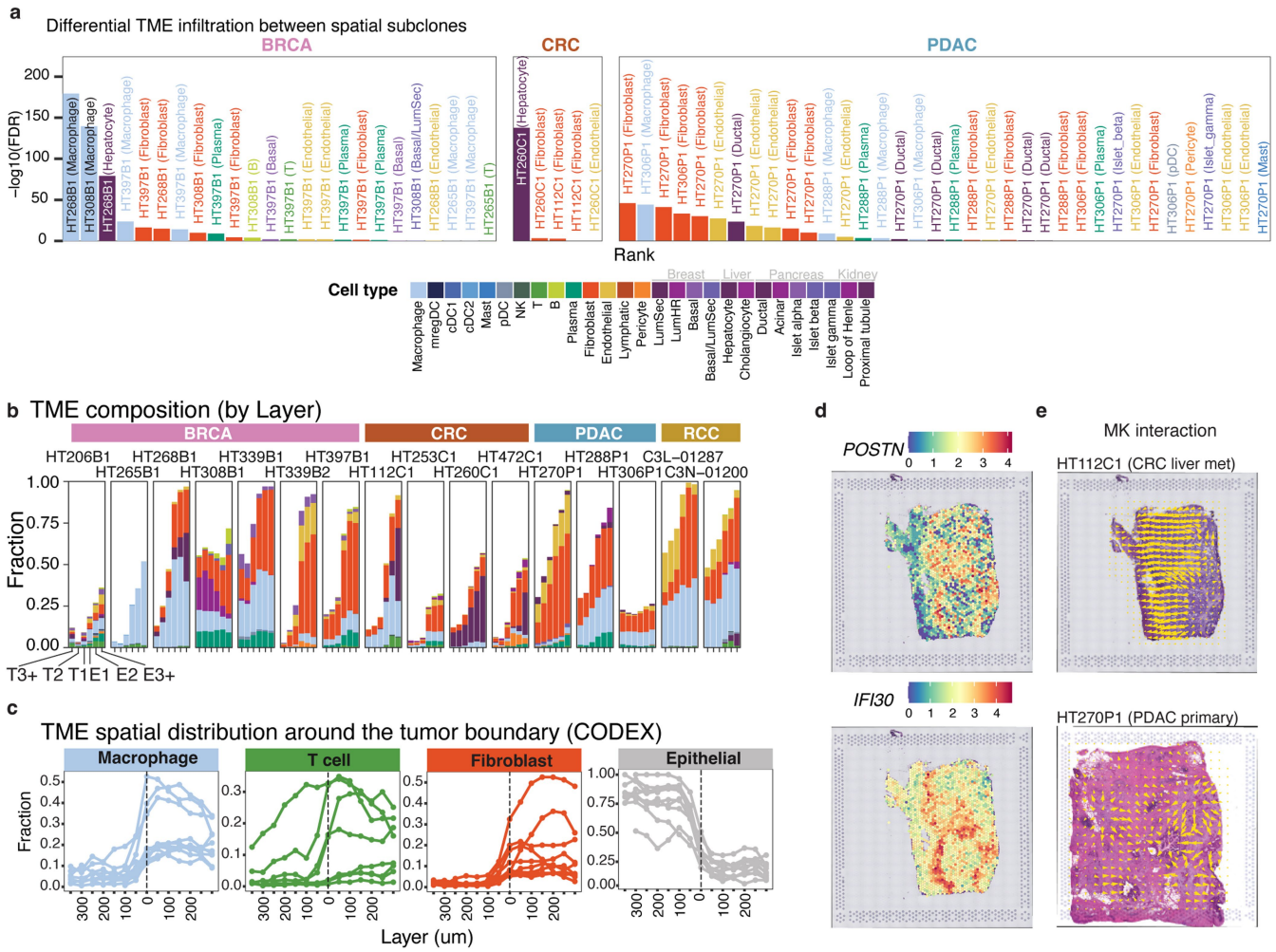

Extended Data Fig. 9 | Spatial Subclone Infiltration and Cell Composition Across Tumor Layers. a, FDR statistics of comparing infiltration level by cell type between any two pairs of spatial subclones on the same sample. All significant FDR (<0.05) of the cell type from each sample was shown here indicating differential infiltration is observed (n = 16 spatially distinct cases with available matching deconvolution). **b**, Cell type composition of 6 regions defined by the following layers, T3 and above (T3+), T2, T1, E1, E2, and E3 and above (E3+), in 16 cases. **c**, Fraction of macrophage, T cell, fibroblast, and tumor in CODEX across 6 regions defined by the following layers, T3 and above, T2, T1, E1, E2, and E3 and above. Each data point represents one sample and data points from the same sample are connected. **d**, Spatial expression of boundary-enriched genes *POSTN* and *IFI30*. **e**, Example cell-cell interactions in MK pathway (*MDK*) in two tumor sections, with the arrow direction indicating signal direction and the arrow length indicating signal strength.

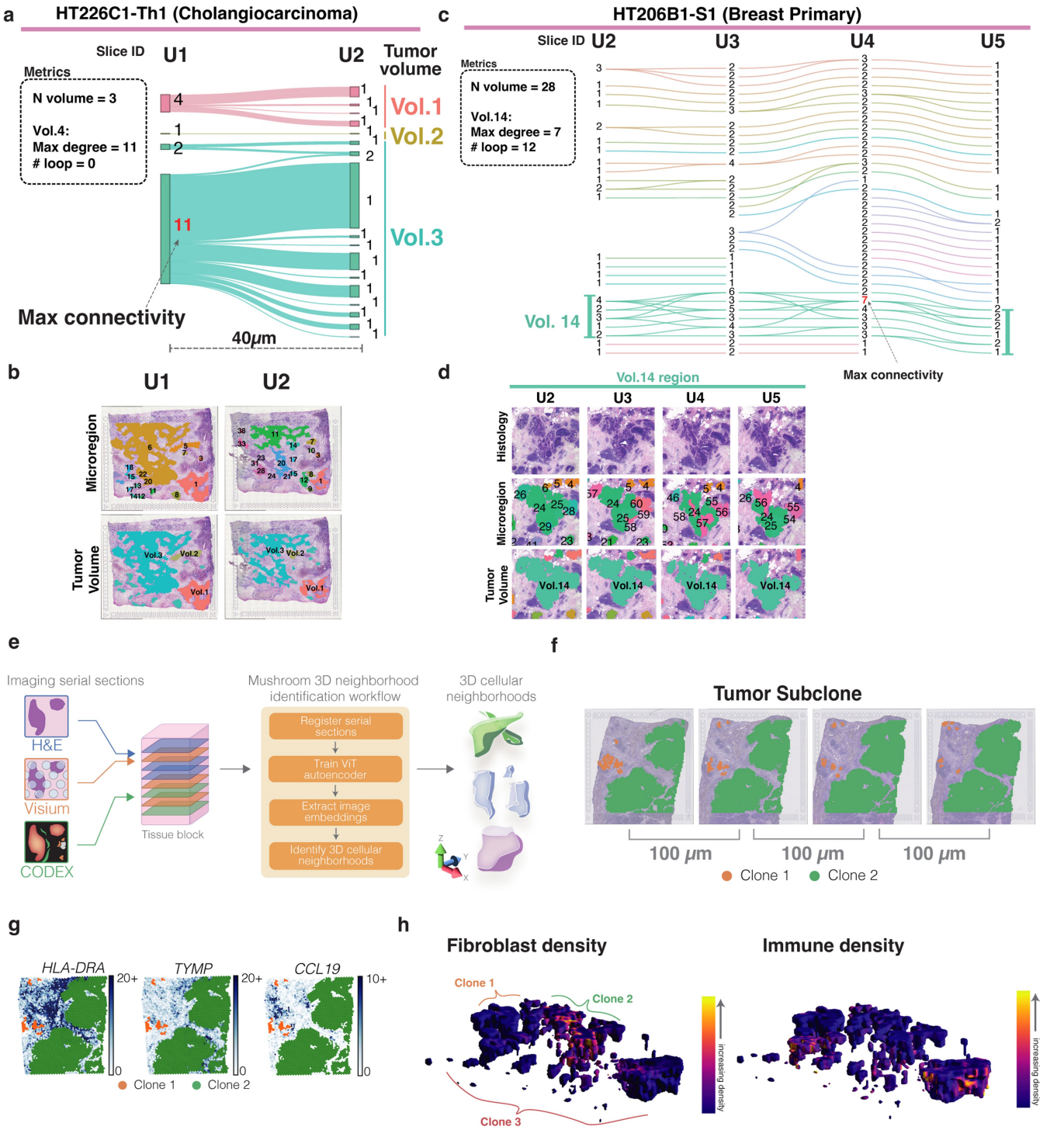

Extended Data Fig. 10 | Spatial Mapping and 3D Reconstruction of Tumor Microregions. a, Analogous Sankey plot and **b**, tumor volume spatial distributions on the ST sections for tissue block HT226C1-Th1. **c**, Analogous Sankey plot and. **d**, Histology, spatial tumor microregion, and distribution of tumor volume Vol.14 in HT206B1-S1. **e**, Overview of the spatial neighborhood identification workflow. Briefly, serial sections are registered and then used to train a vision transformer (ViT) autoencoder that produces image patch embeddings that are assigned to neighborhoods and assembled into 3-dimensional volumes. **f**, Visium ST for HT268B1 overlaid with copy number subclone annotations with distance in microns shown between sections. **g**, Spatial expression of additional DEGs corresponding to TME neighborhoods 4 (*TYMP*), 6 (*CCL9*), and shared (*HLA-DRA*) genes. **h**, 3D reconstruction of tumor regions for HT397B1. The tumor surface mesh is colored by the density of fibroblasts and immune cells within a 50-micron radius of a given location.

nature portfolio

Corresponding author(s): Li Ding, Feng Chen, Benjamin J. Raphael, Ryan C. Fields, William E. Gillanders

Last updated by author(s): Aug 12, 2024

Reporting Summary

Nature Portfolio wishes to improve the reproducibility of the work that we publish. This form provides structure for consistency and transparency in reporting. For further information on Nature Portfolio policies, see our Editorial Policies and the Editorial Policy Checklist.

Statistics

For all statistical analyses, confirm that the following items are present in the figure legend, table legend, main text, or Methods section.

n/a	Confirmed
☐	☒ The exact sample size (*n*) for each experimental group/condition, given as a discrete number and unit of measurement
☐	☒ A statement on whether measurements were taken from distinct samples or whether the same sample was measured repeatedly
☐	☒ The statistical test(s) used AND whether they are one- or two-sided *Only common tests should be described solely by name; describe more complex techniques in the Methods section.*
☐	☒ A description of all covariates tested
☐	☒ A description of any assumptions or corrections, such as tests of normality and adjustment for multiple comparisons
☐	☒ A full description of the statistical parameters including central tendency (e.g. means) or other basic estimates (e.g. regression coefficient) AND variation (e.g. standard deviation) or associated estimates of uncertainty (e.g. confidence intervals)
☐	☒ For null hypothesis testing, the test statistic (e.g. *F*, *t*, *r*) with confidence intervals, effect sizes, degrees of freedom and *P* value noted *Give P values as exact values whenever suitable.*
☒	☐ For Bayesian analysis, information on the choice of priors and Markov chain Monte Carlo settings
☒	☐ For hierarchical and complex designs, identification of the appropriate level for tests and full reporting of outcomes
☐	☒ Estimates of effect sizes (e.g. Cohen's *d*, Pearson's *r*), indicating how they were calculated

Our web collection on statistics for biologists contains articles on many of the points above.

Software and code

Policy information about availability of computer code

Data collection	No software was used for data collection
Data analysis	Mushroom, https://github.com/ding-lab/mushroom/tree/subclone_submission Morph, https://github.com/ding-lab/morph multiplex imaging pipeline, https://github.com/estorrs/multiplex-imaging-pipeline Space Ranger v1.3.0, v 2.0.0, v2.1.0, 10X Genomics Cell Ranger v6.0.2, 10X Genomics InferCNV v1.10.1, https://github.com/broadinstitute/infercnv CalicoST, https://github.com/raphael-group/CalicoST 10Xmapping, https://github.com/ding-lab/10Xmapping samtools v1.14, https://github.com/samtools/samtools trimGalore v.0.6.7, https://github.com/FelixKrueger/TrimGalore BWA-mem v0.7.17, https://github.com/lh3/bwa Somaticwrapper v2.2, https://github.com/ding-lab/somaticwrapper Picard v2.6.26, https://github.com/broadinstitute/picard Strelka v2.9.10, https://github.com/Illumina/strelka MUTECT v1.1.7, https://github.com/broadinstitute/mutect VarScan v2.3.8, https://dkoboldt.github.io/varscan Pindel v0.2.5, https://github.com/genome/pindel COCOON, https://github.com/ding-lab/COCOONS scVarScan, https://github.com/ding-lab/10Xmapping

GATK v4.1.9.0, https://github.com/broadinstitute/gatk
Bedtools 2.30.0, https://github.com/arq5x/bedtools2
Scrublet v0.2.3, https://github.com/swolock/scrublet
Seurat v4.3.0, R-package
ComplexHeatmap v2.14.0, R-package
tidyverse v1.3.2, R-package
ggplot2 v3.3.5, R-package
RColorBrewer v1.1.3, R-package
singleR v1.8.1, R-package
clusterProfiler v3.18.1, R-package
msigdbr v7.5.1, R-package
ROGUE v1.0, R-package
RCTD v1.2.0, R-package
COMMOT, https://github.com/zcang/COMMOT
PASTE2, https://github.com/raphael-group/paste2
ppcor v1.1, R-package
stats v4.1.2, R-package
ggpubr v0.6.0, R-package
python v3.7.12 and v.3.9.6
sklearn v0.24.2, python-package
matplotlib v3.4.2, py39hf3d152e_0
numpy v1.21.1, h49503c6_1_cpython
org.Hs.eg.db v3.12.0, R-package
pandas v1.3.1, py39hde0f152_0
Fiji/ImageJ, v2.14.0
BigWarp, Figi/ImageJ-package
Napari v0.4.19
Imaris v10.1.1
DeepCell v0.12.9, https://github.com/vanvalenlab/deepcell-tf

For manuscripts utilizing custom algorithms or software that are central to the research but not yet described in published literature, software must be made available to editors and reviewers. We strongly encourage code deposition in a community repository (e.g. GitHub). See the Nature Portfolio guidelines for submitting code & software for further information.

Data

Policy information about availability of data

All manuscripts must include a data availability statement. This statement should provide the following information, where applicable:

- Accession codes, unique identifiers, or web links for publicly available datasets
- A description of any restrictions on data availability
- For clinical datasets or third party data, please ensure that the statement adheres to our policy

Visium, sc/snRNA-seq, WES, Xenium, and CODEX imaging data are part of Human Tumor Atlas Network (HTAN) dbGaP Study Accession: phs002371.v3.p1 (https://www.ncbi.nlm.nih.gov/projects/gap/cgi-bin/study.cgi?study_id=phs002371.v3.p1), and the Data can be accessed through the HTAN DCC Portal (https://data.humantumoratlas.org/) under the HTAN WUSTL Atlas. Individual samples can be identify using Biospecimen ID from the Sample_ID_Lookup_table.xlsx on the GitHub page (https://github.com/ding-lab/ST_subclone_publication). GRCh38 references used for sc/snRNA-seq (refdata-gex-GRCh38-2020-A) is freely available from 10X Genomics website (https://support.10xgenomics.com). The reference GRCh38 genome (GRCh38.d1.vd1.fa.tar.gz) used for WES reads alignment is available from GDC (https://gdc.cancer.gov/about-data/gdc-data-processing/gdc-reference-files). The MSigDB hallmark gene sets is available from GSEA website (https://www.gsea-msigdb.org/gsea/msigdb/collections.jsp). The L1000 perturbation database is available through the resource page on the Harmonizome website (https://maayanlab.cloud/Harmonizome/resource/LINCS+L1000+Connectivity+Map) and the library page on the Enrichr website (https://maayanlab.cloud/Enrichr/#libraries).

Research involving human participants, their data, or biological material

Policy information about studies with human participants or human data. See also policy information about sex, gender (identity/presentation), and sexual orientation and race, ethnicity and racism.

Reporting on sex and gender	Patient sex information was collected as part of this study
Reporting on race, ethnicity, or other socially relevant groupings	Patient race or ethnicity information was collected as part of this study
Population characteristics	Our dataset comprises samples from 6 tumor types, with patients ages 37-82. The distribution of the samples and clinical information across the cohorts can be found in the Supplementary Table 1, and Extended Data Fig. 1a.
Recruitment	Patients who fit the clinical criteria and consented to the study were selected for inclusion in the genetic and molecular tumor analysis. 75 cases from 6 cancers are part of Human Tumor Atlas Network (HTAN) study, and 3 ccRCC cases are from Clinical (Clinical Proteomic Tumor Analysis Consortium). There was no self-selection bias or other biases in the recruitment of patients
Ethics oversight	All samples were collected with informed consent at the Washington University School of Medicine in St Louis. Breast cancer

Ethics oversight	(BRCA) samples, pancreatic adenocarcinoma (PDAC) samples, colorectal cancer (CRC) samples, cholangiocarcinoma (CHOL) samples, renal carcinoma (RCC) samples and uterine corpus endometrial carcinoma (UCEC) samples were collected during surgical resection and verified by standard pathology (IRB protocol 201108117, 201411135, and 202106166). Tumor samples were collected during surgical resection and verified by standard pathology.

Note that full information on the approval of the study protocol must also be provided in the manuscript.

Field-specific reporting

Please select the one below that is the best fit for your research. If you are not sure, read the appropriate sections before making your selection.

☒ Life sciences ☐ Behavioural & social sciences ☐ Ecological, evolutionary & environmental sciences

For a reference copy of the document with all sections, see nature.com/documents/nr-reporting-summary-flat.pdf

Life sciences study design

All studies must disclose on these points even when the disclosure is negative.

Sample size	Sample sizes were chosen based on the availability of samples collected across 6 cancer types. No specific statistical methods were used to predetermine sample size. This cohort collected a total of 132 sections from 79 cases samples for Visium ST, along with several samples for paired snRNA-seq, WES, and CODEX. This sample size aligns with or exceeds that of many previously published Visium spatial transcriptomics data on the date of submission.
Data exclusions	No data were excluded from the analysis
Replication	To ensure reproducibility, we used multiple bioinformatics tools for the same analyses and compared results across technologies (including bulk, single-cell, spatial sequencing, and multiplexed imaging) from the same tumor samples. To confirm subclonal copy number alterations in tumor spatial regions, we used two independent copy number inference methods, CalicoST (github.com/raphael-group/CalicoST) and InferCNV (https://github.com/broadinstitute/infercnv) (Supplementary Fig. 5a). We further validated spatial CNV inference with matching WES-based CNV calling and observed 0.43-0.82 agreement in Jaccard similarity (methods) between the dominant spatial subclone and WES (Supplementary Fig. 5c). Further, spatial subclonal mutations were validated with matching WES-based mutation calling (with 4%-33% WES mutations detected in spatial transcriptomics, Supplementary Fig. 5d). To support our findings in the tumor center and periphery regions, we used matching snRNA-seq from the same tumor samples and demonstrated expression of most center-enriched and periphery-enriched genes in malignant cells (Supplementary Fig. 8a). Subclonal tumor microenvironment compositions were confirmed with multiplexed immunostaining with co-detection by indexing (CODEX) (Fig. 5c).
Randomization	The study design didn't involve the allocation of patients into treatment groups, therefore the randomization procedure was not relevant.
Blinding	The study design didn't involve the allocation of patients into treatment groups, therefore blinding procedure was not relevant.

Reporting for specific materials, systems and methods

We require information from authors about some types of materials, experimental systems and methods used in many studies. Here, indicate whether each material, system or method listed is relevant to your study. If you are not sure if a list item applies to your research, read the appropriate section before selecting a response.

Materials & experimental systems

n/a	Involved in the study
☐	☒ Antibodies
☒	☐ Eukaryotic cell lines
☒	☐ Palaeontology and archaeology
☒	☐ Animals and other organisms
☒	☐ Clinical data
☒	☐ Dual use research of concern
☒	☐ Plants

Methods

n/a	Involved in the study
☒	☐ ChIP-seq
☒	☐ Flow cytometry
☒	☐ MRI-based neuroimaging

Antibodies

Antibodies used	CD11b (Abcam #ab187537;EP1345Y),CD20 (Abcam #ab236434;SP32),CD31 (Abcam #ab226157;EP3095),CD68 (Abcam #ab233172;KP1),CK19 (Abcam #ab195872;EP1580Y),GLUT1 (Abcam #ab196357;EPR3915),CD163 (Akoya #4250079;AKYP0114),CD3e (Akoya #4550125;EP449E),CD4 (Akoya #4550112;EPR6855),CD8 (Akoya #4250012;C8/144B),FOXP3 (Akoya #4550071;AKYP0102),HLA-DR (Akoya #4450095;EPR3692),Ki67 (Akoya #4450096;B56),Pan-Cytokeratin (Akoya #4450093;AE-1/AE-3),Podoplanin (BioLegend #337002;NC-08),Vimentin (BioLegend #677802;O91D3),SMA (Invitrogen #MA1-06110;1A4),CD45 (Novus Biologicals #NBP2-34528;2B11+PD7/26),E-cadherin (Thermofisher #33-4000;4A2C7),AQP1 (Abcam #ab178352;EPR11588(B)),AQP2 (Abcam #ab230170;EPR21080),CALB1 (Abcam #ab233018;EP3478),CK17 (Abcam

#ab239986;EP1623),cKit (Abcam #ab216450;YR145),COX6c (Abcam #ab243916;EPR9938),GATA3 (Abcam #ab214804;EPR16651),Her2 (Abcam #ab194979;EP1045Y),LRP2 (Abcam #ab76969;Polyclonal),MGP (Abcam #ab273657;OTI8D6),MUC2 (Abcam #ab272706;EPR23479-47),P21 (Abcam #ab212247;CIP1/823),PAI1 (Abcam #ab237780;EPR21850-82),PLAT/tPA (Abcam #ab240146;EPR7232(2)),PR (Abcam #ab239793;SP2),SOX9 (Abcam #ab225541;EPR14335-78),UCHL1 (Abcam #ab220823;EPR4118),UMOD (Abcam #ab223540;EPR20071),CK5 (Akoya #4450090;AKYP0121),ER (Akoya #4250074;AKYP0105),CP (Bethyl Laboratories #A80-124A;Polyclonal),CK14 (BioLegend #905304;Polyclonal),MLPH (Invitrogen #PA5-118065;Polyclonal),CA9 (Novus Biologicals #NB100-417;Polyclonal),CCL2 (Novus Biologicals #NBP2-22115;2D8),CK7 (Novus Biologicals #NBP-47940;OV-TL12/30),Hep-Par-1 (Novus Biologicals #NBP2-45272;HepPar1),CD36 (Cell Signaling Technology #39914;D8L9T),TFF1 (Abcam #ab239908;EPR3972)

Validation

Antibodies used in this application have already been used in our laboratory and confirmed by one or more of the following methods. First: Western blotting produces the correct banding pattern (correct molecular weight, absence in non-transfected cells or protein extracts from mice deficient for the gene but present in wild-type samples or samples with transfection of an expression construct). Second, immunostaining shows the correct pattern (correct tissue specificity, intracellular location, absent/low in non-transfected cells, present/high in transfected cells, colocalization with the tags for fusion proteins expressed in cells). Third, 2 or more independent antibodies against the same antigen show the same expected pattern.
In addition, we have included detail antibody information in Supplementary Table_04_CODEX_Antibody.xlsx, further validation images in 2_Response_letter.pdf and 2b_Respons_Ab_IF_testing_0610.pdf

Plants

Seed stocks

Report on the source of all seed stocks or other plant material used. If applicable, state the seed stock centre and catalogue number. If plant specimens were collected from the field, describe the collection location, date and sampling procedures.

Novel plant genotypes

Describe the methods by which all novel plant genotypes were produced. This includes those generated by transgenic approaches, gene editing, chemical/radiation-based mutagenesis and hybridization. For transgenic lines, describe the transformation method, the number of independent lines analyzed and the generation upon which experiments were performed. For gene-edited lines, describe the editor used, the endogenous sequence targeted for editing, the targeting guide RNA sequence (if applicable) and how the editor was applied.

Authentication

Describe any authentication procedures for each seed stock used or novel genotype generated. Describe any experiments used to assess the effect of a mutation and, where applicable, how potential secondary effects (e.g. second site T-DNA insertions, mosiacism, off-target gene editing) were examined.